Biological uptake and reversible scavenging of zinc in the global ocean

One-sentence summary

A new data-constrained model quantifies the roles of circulation, organic matter cycling, and reversible scavenging in the oceanic cycling zinc and its isotopes, with implications for trace metal limitation of phytoplankton ecology in the past, present, and future ocean.

Authors and affiliations

Thomas Weber[1*,a], Seth John[2,a], Alessandro Tagliabue[3], Tim DeVries[4]

[1] Department of Earth and Environmental Sciences, University of Rochester, Rochester, NY, 14618, USA

[2] Department of Earth Sciences, University of Southern California, Los Angeles, CA, 90089, USA.

[3] School of Environmental Sciences, University of Liverpool, Liverpool, UK

[4] Department of Geography and Earth Research Institute, University of California, Santa Barbara, CA USA

[*] Correspondence to T.W. (t.weber@rochester.edu)

[a] These authors contributed equally to this work

Abstract

Zinc (Zn) is a key micronutrient for marine phytoplankton, with a global distribution that is remarkably similar to silicic acid. The processes that govern this relationship, despite the very different biological cycling of Zn and silica, remain poorly understood. Here we use diagnostic and mechanistic models to show that only a combination of Southern Ocean biological uptake and reversible scavenging of Zn onto sinking particles can explain the observations. The distinction between organic and adsorbed Zn can also reconcile the vertical distribution and mass balance of Zn isotopes, which previously appeared at odds. This holistic understanding explains the Zn deficiencies observed throughout the low latitude ocean, and implies a greater sensitivity of the marine Zn cycle to climate-driven changes in organic matter cycling than previously recognized.

Main Text

Zn is the second most abundant micronutrient in phytoplankton biomass (*1*) with fundamental roles in DNA replication and transcription, and as a cofactor in carbonic anhydrase and alkaline phosphatase enzymes (*2*). Since the earliest trace metal clean observations (*3*), and further exemplified by the global GEOTRACES program (*4*), a close correlation between the oceanic distributions of Zn and silicic acid ($Si(OH)_4$, Si hereafter) has been observed (Fig. 1a). Like Si, Zn is systematically enriched in deep watermasses and deficient in intermediate watermasses relative to other algal nutrients such as phosphate (PO_4^{3-}). This results in widespread Zn scarcity throughout low latitude ocean, potentially impacting biological activity and plankton community structure, particularly in low PO_4^{3-} regions (*5, 6*).

The spatial covariation of Zn and Si is surprising given their distinct biogeochemical cycles. Si is assimilated by diatoms and used to build external opal frustules, whereas Zn is assimilated by all phytoplankton taxa, with cellular quotas that scale with Zn availability up to ~10mmol Zn per mol P (*7*). Only 1-3% of cellular Zn is directly incorporated into the frustules of cultured diatoms (*8*), while the vast majority is co-located with phosphorus (P) in internal organelles (*1*). Zn is released from decomposing organic particles at the same rate as P (*9*), and both are released shallower in the water column than Si (*10, 11*). These observations suggest a fundamental decoupling between Zn and Si during the vertical cycling of organic matter that appears at odds with their correlated ocean concentrations (Fig. 1a). Identifying the "missing" processes that facilitate this linkage is essential to understand the climate sensitivity of the marine Zn cycle.

Recently, it has been hypothesized that the global Zn/Si covariation emerges from physical coupling in the Southern Ocean (*12*). As upwelling deep water flows northwards in the region, surface Zn and Si are exhausted earlier than PO_4^{3-} (*13*). This results in a band of Zn and Si-deficient water in the Polar Frontal Zone that is subducted northwards within Antarctic Intermediate Water (AAIW), while Zn and Si remain enriched in Antarctic Bottom Water (AABW) that flows north from Antarctica at greater depth (*14*). Because these watermasses ventilate much of the ocean interior, the stoichiometry of

their formation regions is thought to propagate globally and overwhelm differences in organic Zn and Si cycling.

If the "Southern Ocean hypothesis" is complete, Zn concentrations must be modified very little as watermasses spread northwards beyond the Southern Ocean. Any significant accumulation of remineralized Zn would drive a shallower concentration maximum, making the Zn distribution diverge from Si and converge towards PO_4^{3-}.

We tested this hypothesis from an observational perspective by taking a representative observed profile of [Zn] from the North Pacific Ocean (Fig. 1b) and dividing it analytically into two components. The first component represents the quantity of Zn transported from the Southern Ocean to the North Pacific site (Fig 1c), and was computed using a data constrained ocean circulation model to propagate the Zn distribution of the Southern Ocean (statistically mapped south of 40°S) throughout the Pacific Ocean interior (*15*). The difference between the circulated component and the observed [Zn] then quantifies the additional Zn that has accumulated during northward transport from the Southern Ocean, e.g. from remineralization or other internal cycling processes (Fig. 1d).

Our analysis reveals only ~6nM (~65%) of the observed Zn in the deep North Pacific is accounted for by circulation from the Southern Ocean (Fig 1c). Therefore ~3nM (~35%) is unaccounted for and must have accumulated since these waters passed 40°S (Fig. 1d). Conducting a similar exercise for Si and PO_4^{3-} profiles (*15*) reveals that the accumulated Zn component does not share the same depth profile as accumulated PO_4^{3-}, which reaches a shallow peak centered around ~800m, but rather exhibits a broad deep peak between 1000-3000m, similar to accumulated Si (Fig 1d). The same pattern is found repeating this analysis in the Tropical Pacific (Fig. S1).

To further assess the role of the Southern Ocean, we developed a mechanistic model of global PO_4^{3-}, Zn and Si cycling embedded within our data-constrained circulation model (*15*). Surface [PO_4^{3-}] and [Si] are restored towards observations to quantify the export of particulate organic P and biogenic Si, which remineralize over depth scales that were optimized to best match observed global PO_4^{3-} and Si distributions (Fig. S2, Table S1). Zn complexation by organic ligands is represented by an equilibrium model (*16*), and biological uptake of uncomplexed Zn is coupled to PO_4^{3-} in a ratio that

increases with [Zn] (*7*). Particulate organic Zn is assumed to remineralize over the same depth scale as organic P. Four parameters governing Zn complexation and uptake were optimized to best fit a range of observational constraints (*4*), including a Southern Ocean surface [Zn] transect and profiles from the Atlantic, Pacific, Indian and Southern Oceans (Fig. S3, Table S2). The optimization procedure is an important facet of our approach, allowing us to interpret remaining model-data discrepancies as genuine model deficiencies, rather than poor parameter choices.

Our optimized model produces a near-linear relationship between Zn and Si (Fig. 2a) when Southern Ocean surface [Zn] is accurately reproduced (Fig. 2b). However, the correlation (R^2=0.86) is weaker than observed (R^2=0.95) and systematic biases are evident, contrary to results of a previous modeling study (*12*). Modelled [Zn] is overestimated at low Si concentrations in intermediate watermasses (Fig. 2a,c), and underestimated in deep waters of the Pacific and Indian Oceans (Fig. 2c, S3). Furthermore, our model requires Zn:P export ratios approaching 20mmol:1mol in order to sufficiently deplete [Zn] in the Southern Ocean (Fig. 2b, S4), which exceeds the observed biological range (*1*).

Taken together, our diagnostic results and mechanistic modeling demonstrate that Southern Ocean uptake and circulation are important but insufficient factors to explain the global Zn distribution. Soft organic tissue cycling causes Zn to accumulate too shallow in the watercolumn, indicating that an additional process is required explain the deep accumulation pattern (Fig. 1d). Model sensitivity tests indicate that neither hydrothermal Zn inputs (*17*) nor spatially-varying remineralization scales of organic matter (*18*) can resolve the discrepancy (Fig. S5). A candidate hypothesis, supported by laboratory culture studies, is that Zn is reversibly "scavenged" (adsorbed) onto sinking organic particles, enhancing its flux to the deep ocean relative to non-scavenged elements like P (*9*).

We tested whether a second model configuration that explicitly includes reversible scavenging (*15*) can reconcile the Si-like distribution of Zn with its P-like remineralization behavior. The model computes the equilibrium partitioning of uncomplexed Zn between the dissolved phase and a phase adsorbed to sinking particulate organic matter based on a globally uniform partition coefficient (*19*), and does not

consider potential adsorption to mineral phases. Following parameter optimization, this model successfully reproduces the observed tight correlation between Zn and Si (R^2=0.98), without leaving systematic biases (Fig. 2d). While Zn concentrations in the surface Southern Ocean remain unchanged from the original model (Fig. 2e), scavenging redistributes Zn from intermediate to deep watermasses as they age, bringing its simulated depth structure in line with observations (Fig 2f, S3). This occurs even though only a small fraction of total Zn is adsorbed onto particles: ~0.5% in the upper ocean and <0.01% in the deep ocean (Fig. S6). Overall, resolving reversible scavenging reduces the RMS error between simulated and observed Zn by a factor of ~2 relative to the original model (0.59nM vs. 1.03nM, Table S3). Additionally, inclusion of scavenging permits realistic surface depletion without the excessive Zn:P export ratios seen in our earlier model (Fig. 2e, S4). Model sensitivity tests demonstrate that reversible scavenging must be active throughout the water column, and not confined to low oxygen waters, to best match the observations (Fig S5). This suggests that the scavenging mechanism is not related to trace metal sulfide precipitation in particle microenvironments (*20*), which might be more important at smaller scales and for other metals such as Cadmium.

By linking Southern Ocean watermasses with reversible scavenging, our model provides a holistic understanding of the oceanic Zn cycle and its relationships to Si and PO_4^{3-}. The roles of physical and biogechemical processes can be isolated using stoichiometric tracers that measure the excess or deficit of Zn and Si relative to PO_4^{3-}. Here, we define Zn_{xs}=[Zn]-$R_{Zn:P}$[PO_4^{3-}] and Si_{xs}=[Si]-$R_{Si:P}$[PO_4^{3-}], where $R_{Zn;P}$ and $R_{Si:P}$ represent mean-ocean elemental ratios. Nutrient utilization in the Southern Ocean surface produces watermasses with distinct stoichiometries that are conserved by circulation: AAIW carries strongly negative Zn_{xs} (-1.5nM) and Si_{xs} (-40μM) into low latitudes, whereas deeper AABW carries weakly positive values (Fig. 3a).

Modification of these tracers along circulation pathways reflects biogeochemical processes that decouple Zn and Si from PO_4^{3-}. Si_{xs} decreases in AAIW as it ages equatorward and increases in AABW (Fig. 3a), reflecting remineralization of P in intermediate waters and excess Si remineralization in the deep ocean (Fig 3b) (*11*). Zn_{xs} undergoes almost identical modifications (Fig. 3a), but via a different set of mechanisms. In the upper ~400m where organic Zn remineralizes rapidly like P, net adsorption

transfers dissolved Zn onto particles (Fig. 3b), constituting a sink of Zn_{xs}. Deeper, the equilibrium between adsorbed and dissolved Zn shifts due to lower particle concentrations, driving net desorption and accumulation of Zn, relative to PO_4^{3-} in AABW (Fig. 3a). Outside the Southern Ocean, the combined flux profiles of organic and adsorbed Zn are more similar to Si than P, with ~30% of Zn transferred from the base of the euphotic zone to 2000m, compared to ~40% and ~5% for Si and P respectively (Fig. 3b). By the time AABW reaches the North Pacific Ocean, the accumulation of desorbed Zn adds ~2nM to the concentration leaving the Southern Ocean in AABW, compared to ~1nM accumulated from remineralization (Fig. 3c), demonstrating that reversible scavenging is a critical process explaining the deep accumulation of Zn (Fig. 1d).

In our optimized model, removing the reversible scavenging process and preventing elevated uptake of Zn in the Southern Ocean degrade the fit to observations to a similar degree (*15*). This suggests that both processes are equally responsible for decoupling the Zn distribution from other soft tissue nutrients, and its global similarity to Si. Nevertheless, in young watermasses that have not undergone extensive scavenging, shallow remineralization of Zn can locally decouple its concentration from Si (Fig. S3), as observed in the Subarctic North Pacific Ocean (*21*), although the mechanism for this decoupling was not previously clear.

The existence of distinct organic and adsorbed sinking Zn phases can also resolve an apparent conflict between the vertical distribution of Zn isotopes, and the isotopic mass balance of the ocean as a whole. In the low latitude ocean, the ratio of ^{66}Zn to ^{64}Zn (expressed as $\delta^{66}Zn$) decreases towards the surface, implying preferential removal of heavy isotopes from the upper ocean and their transfer to depth (Fig. 4a)(*22*). However, light isotopes must be preferentially buried from the ocean as a whole to balance fluvial, atmospheric and hydrothermal sources that are isotopically light (0.3-0.35‰) relative to mean-ocean Zn (~0.5‰) (*23*).

We expanded our global model to distinguish the cycles of ^{66}Zn and ^{64}Zn, which are fractionated during biological uptake, complexation, and scavenging (*15*), and the magnitude of each fractionation effect was optimized within reasonable ranges to match observed $\delta^{66}Zn$ profiles (Fig. 4a, S7). In the optimal model, ^{66}Zn is preferentially adsorbed onto sinking particles due to its weaker binding by ligands, consistent with

culture studies (*9*) and new observations from the Subtropical Pacific (*15*). This fractionation is strongest in the upper 1000m where ligand binding is most complete (Fig. S6, S8). The flux of heavy adsorbed Zn from the upper ocean then leaves a light δ^{66}Zn signature that is transferred into sinking organic matter when phytoplankton consume residual Zn in the surface (Fig. 4b, S8). The δ^{66}Zn of the sinking Zn flux is therefore light (<0.5‰) in the upper ~500m where organic Zn dominates, and heavy (>0.5‰) in deeper layers where the adsorbed flux is dominant (Fig. 4b). Because particulate matter is disproportionately buried on shallow continental shelves (*24*), our model predicts a negative relationship between δ^{66}Zn flux to the seafloor and burial rate (Fig. 4c, S9, *15*), consistent with observations of light Zn burial on Pacific shelves (*25*). Integrated globally this yields a δ^{66}Zn sink of 0.36‰±0.04‰ that is in balance with source estimates (*23*).

Our findings have important implications for Zn biogeochemical cycling in past and future oceans. The geological record exhibits millennial cycles (*26, 27*) and billion-year trends (*28*) in δ^{66}Zn, currently attributed to Zn speciation and changes in biological productivity. Our findings suggest that changes in the relative burial of adsorbed and organic Zn are an important mechanism controlling mean-ocean δ^{66}Zn on geological timescales. In the modern ocean, deep remineralization of Si and reversible scavenging of Zn produce remarkably similar accumulation patterns of the two nutrients, but these processes likely have unique sensitivities to ocean change. While Si cycling will respond to changing ocean temperature and pH (*29*), Zn will be sensitive to projected variations in organic carbon fluxes (*30*) that underpin Zn scavenging, potentially decoupling the Zn and Si supply to low latitude phytoplankton communities.

References and Notes

1. B. S. Twining, S. B. Baines, The trace metal composition of marine phytoplankton. *Annual review of marine science* **5**, 191-215 (2013).
2. F. M. M. Morel *et al.*, Zinc and Carbon Co-Limitation of Marine-Phytoplankton. *Nature* **369**, 740-742 (1994).
3. K. W. Bruland, G. A. Knauer, J. H. Martin, Zinc in Northeast Pacific Water. *Nature* **271**, 741-743 (1978).
4. E. Mawji *et al.*, The GEOTRACES Intermediate Data Product 2014. *Marine Chemistry* **177**, 1-8 (2015).
5. C. Mahaffey, S. Reynolds, C. E. Davis, M. C. Lohan, Alkaline phosphatase activity in the subtropical ocean: insights from nutrient, dust and trace metal addition experiments. *Frontiers in Marine Science* **1**, (2014).
6. Y. Shaked, Y. Xu, K. Leblanc, F. M. M. Morel, Zinc availability and alkaline phosphatase activity in Emiliania huxleyi: Implications for Zn-P co-limitation in the ocean. *Limnology and Oceanography* **51**, 299-309 (2006).
7. W. G. Sunda, S. A. Huntsman, Feedback Interactions between Zinc and Phytoplankton in Seawater. *Limnology and Oceanography* **37**, 25-40 (1992).
8. M. J. Ellwood, K. a. Hunter, The incorporation of zinc and iron into the frustule of the marine diatom Thalassiosira pseudonana. *Limnology and Oceanography* **45**, 1517-1524 (2000).
9. S. G. John, T. M. Conway, A role for scavenging in the marine biogeochemical cycling of zinc and zinc isotopes. *Earth and Planetary Science Letters* **394**, 159-167 (2014).
10. B. Twining, S. Nodder, A. King, Differential remineralization of major and trace elements in sinking diatoms. *Limnol. Oceanogr* **59**, 689-704 (2014).
11. M. Holzer, F. W. Primeau, T. DeVries, R. Matear, The Southern Ocean silicon trap: Data-constrained estimates of regenerated silicic acid, trapping efficiencies, and global transport paths. *Journal of Geophysical Research: Oceans* **119**, 313-331 (2014).
12. D. Vance *et al.*, Silicon and zinc biogeochemical cycles coupled through the Southern Ocean. 1-6 (2017).
13. Y. Zhao, D. Vance, W. Abouchami, H. J. W. de Baar, Biogeochemical cycling of zinc and its isotopes in the Southern Ocean. *Geochimica et Cosmochimica Acta* **125**, 653-672 (2014).
14. J. L. Sarmiento, N. Gruber, M. a. Brzezinski, J. P. Dunne, High-latitude controls of thermocline nutrients and low latitude biological productivity. *Nature* **427**, 56-60 (2004).
15. Materials and methods are available as supplementary materials at the Science website
16. T. Kim, H. Obata, Y. Kondo, H. Ogawa, T. Gamo, Distribution and speciation of dissolved zinc in the western North Pacific and its adjacent seas. *Marine Chemistry* **173**, 330-341 (2015).
17. S. Roshan, J. Wu, W. Jenkins, *Long-range transport of hydrothermal dissolved Zn in the tropical South Pacific*. (2016), vol. 183.

18. T. Weber, J. A. Cram, S. W. Leung, T. DeVries, C. Deutsch, Deep ocean nutrients imply large latitudinal variation in particle transfer efficiency. *Proceedings of the National Academy of Sciences*, 201604414 (2016).
19. M. P. Bacon, R. F. Anderson, Distribution of Thorium Isotopes Between Particulate Forms in The Deep Sea. *Journal of Geophysical Research* **87**, 2045-2056 (1982).
20. D. J. Janssen *et al.*, Undocumented water column sink for cadmium in open ocean oxygen-deficient zones. *Proceedings of the National Academy of Sciences* **111**, 6888-6893 (2014).
21. D. J. Janssen, J. T. Cullen, Decoupling of zinc and silicic acid in the subarctic northeast Pacific interior. *Marine Chemistry* **177**, 124-133 (2015).
22. T. M. Conway, S. G. John, The biogeochemical cycling of zinc and zinc isotopes in the North Atlantic Ocean. *Global Biogeochemical Cycles* **28**, 1111-1128 (2014).
23. S. H. Little, D. Vance, C. Walker-Brown, W. M. Landing, The oceanic mass balance of copper and zinc isotopes, investigated by analysis of their inputs, and outputs to ferromanganese oxide sediments. *Geochimica Et Cosmochimica Acta* **125**, 673-693 (2014).
24. J. P. Dunne, J. L. Sarmiento, A. Gnanadesikan, A synthesis of global particle export from the surface ocean and cycling through the ocean interior and on the seafloor. **21**, 1-16 (2007).
25. S. H. Little, D. Vance, J. McManus, S. Severmann, Key role of continental margin sediments in the oceanic mass balance of Zn and Zn isotopes. *Geology* **44**, 207-210 (2016).
26. S. Pichat, C. Douchet, F. Albarede, Zinc isotope variations in deep-sea carbonates from the eastern equatorial Pacific over the last 175 ka. *Earth and Planetary Science Letters* **210**, 167-178 (2003).
27. M. Kunzmann *et al.*, Zn isotope evidence for immediate resumption of primary productivity after snowball Earth. *Geology* **41**, 27-30 (2013).
28. M. L. Pons *et al.*, A Zn isotope perspective on the rise of continents. *Geobiology* **11**, 201-214 (2013).
29. M. A. Brzezinski, D. M. Nelson, The Annual Silica Cycle in the Sargasso Sea near Bermuda. *Deep-Sea Res Pt I* **42**, 1215-1237 (1995).
30. L. Bopp *et al.*, Multiple stressors of ocean ecosystems in the 21st century: projections with CMIP5 models. (2013).
31. S. G. John, J. Helgoe, E. Townsend, Biogeochemical cycling of Zn and Cd and their stable isotopes in the Eastern Tropical South Pacific. *Marine Chemistry*, (2017).
32. T. DeVries, The oceanic anthropogenic CO2 sink: Storage, air‐sea fluxes, and transports over the industrial era. *Global Biogeochemical Cycles* **28**, 631-647 (2014).
33. S. Khatiwala, A computational framework for simulation of biogeochemical tracers in the ocean. *Global Biogeochemical Cycles* **21**, (2007).
34. H. E. Garcia *et al.*, *World Ocean Atlas 2013, Volume 4 : Dissolved Inorganic Nutrients (phosphate, nitrate, silicate)*. (2013), vol. 4, pp. 27 pp-27 pp.

35. T. DeVries, F. Primeau, Dynamically and Observationally Constrained Estimates of Water-Mass Distributions and Ages in the Global Ocean. *Journal of Physical Oceanography* **41**, 2381-2401 (2011).
36. R. G. Najjar *et al.*, Impact of circulation on export production, dissolved organic matter, and dissolved oxygen in the ocean: Results from Phase II of the Ocean Carbon-cycle Model Intercomparison Project (OCMIP-2). *Global Biogeochemical Cycles* **21**, (2007).
37. J. H. Martin, G. A. Knauer, D. M. Karl, W. W. Broenkow, VERTEX: carbon cycling in the northeast Pacific. *Deep Sea Research Part A, Oceanographic Research Papers* **34**, 267-285 (1987).
38. T. DeVries, J.-H. Liang, C. Deutsch, A mechanistic particle flux model applied to the oceanic phosphorus cycle. *Biogeosciences* **11**, 5381-5398 (2014).
39. P. Parekh, Modeling the global ocean iron cycle. *Global Biogeochemical Cycles* **18**, 1-16 (2004).
40. K. W. Bruland, Complexation of zinc by natural organic ligands in the central North Pacific. *Limnology and Oceanography* **34**, 269-285 (1989).
41. M. Siddall *et al.*, Towards explaining the Nd paradox using reversible scavenging in an ocean general circulation model. *Earth and Planetary Science Letters* **274**, 448-461 (2008).
42. M. Holzer *et al.*, Objective estimates of mantle 3He in the ocean and implications for constraining the deep ocean circulation. *Earth and Planetary Science Letters* **458**, 305 - 314 (2017).
43. C. M. Marsay, R. J. Sanders, S. a. Henson, K. Pabortsava, E. P. Achterberg, Attenuation of sinking particulate organic carbon flux through the mesopelagic ocean. (2014).
44. C. J. Somes *et al.*, Simulating the global distribution of nitrogen isotopes in the ocean. *Global Biogeochemical Cycles* **24**, 1-16 (2010).
45. S. G. John, R. W. Geis, M. a. Saito, E. a. Boyle, Zinc isotope fractionation during high-affinity and low-affinity zinc transport by the marine diatom Thalassiosira oceanica. *Limnology and Oceanography* **52**, 2710-2714 (2007).
46. M. Kobberich, D. Vance, Kinetic control on Zn isotope signatures recorded in marine diatoms. *Geochimica Et Cosmochimica Acta* **210**, 97-113 (2017).
47. R. M. Boiteau, J. N. Fitzsimmons, D. J. Repeta, E. A. Boyle, Detection of Iron Ligands in Seawater and Marine Cyanobacteria Cultures by High-Performance Liquid Chromatography-Inductively Coupled Plasma-Mass Spectrometry. *Analytical Chemistry* **85**, 4357-4362 (2013).
48. T. M. Conway, A. D. Rosenberg, J. F. Adkins, S. G. John, A new method for precise determination of iron, zinc and cadmium stable isotope ratios in seawater by double-spike mass spectrometry (vol 793, pg 44, 2013). *Anal Chim Acta* **801**, 97-97 (2013).
49. T. M. Conway, S. G. John, The cycling of iron, zinc and cadmium in the North East Pacific Ocean - Insights from stable isotopes. *Geochimica Et Cosmochimica Acta* **164**, 262-283 (2015).
50. J. C. Dutay *et al.*, Evaluation of ocean model ventilation with CFC-11: comparison of 13 global ocean models. *Ocean Model* **4**, 89-120 (2002).

51. S. C. Doney *et al.*, Evaluating global ocean carbon models: The importance of realistic physics. *Global Biogeochemical Cycles* **18**, (2004).
52. M. J. Ellwood, C. M. G. Van den Berg, Zinc speciation in the Northeast Atlantic Ocean. *Marine Chemistry* **68**, 295-306 (2000).

Acknowledgements

This work was supported by NSF (OCE-1658042 to T.W., OCE-1649439 and OCE-1658436 to S.J., OCE-1658392 to T.D.), NERC (NE/N001079/1 to A.T.) and the Simons Foundation (329108 to S.J.). We thank Randelle Bundy and Dan Repeta for providing organic Zn samples from the North Pacific for isotope analysis. Data used in this paper is presented in the supplementary materials or available from the GEOTRACES archive (http://www.geotraces.org/). The ocean circulation model is available from (http://www.geog.ucsb.edu/~devries/Home/Models.html).

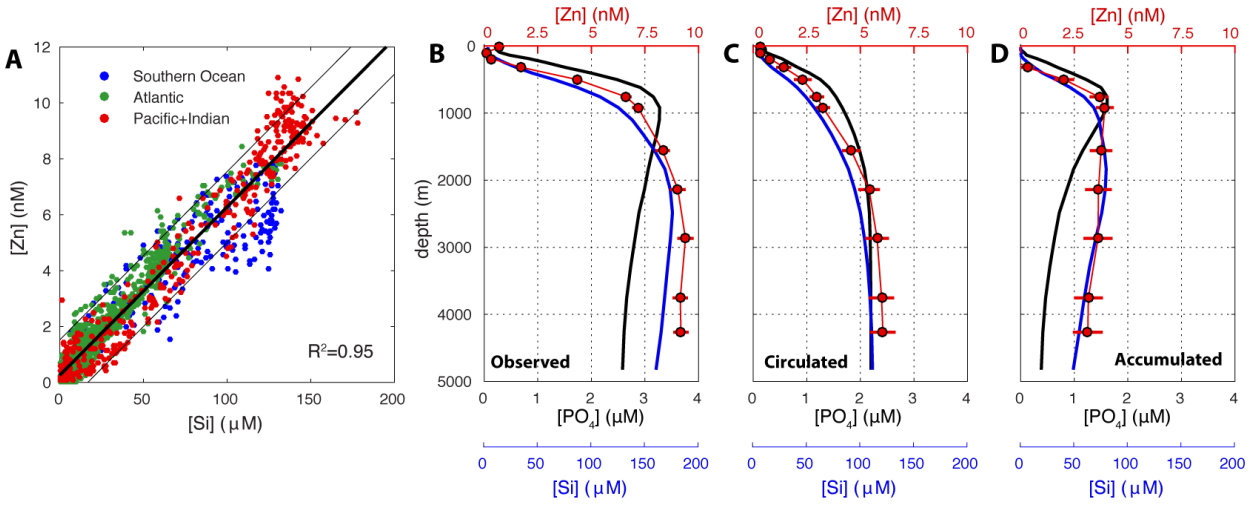

Figure 1. Oceanic Zn distribution and components. A) Scatter plot of observed Zn vs Si, with best fit regression line (thick black line) and 95% prediction intervals (thin black lines). Zn data is from the GEOTRACES IDP 2014 and refs (*9, 21, 31*). **B)** Observed profiles of Zn, Si and PO4 at the SAFe site in the N. Pacific Ocean (*9*). These profiles are divided into a component transported from the Southern Ocean (**C**) and a component accumulated by watermasses since leaving the Southern Ocean (**D**). Uncertainty in each component was quantified using a Monte Carlo method (*15*).

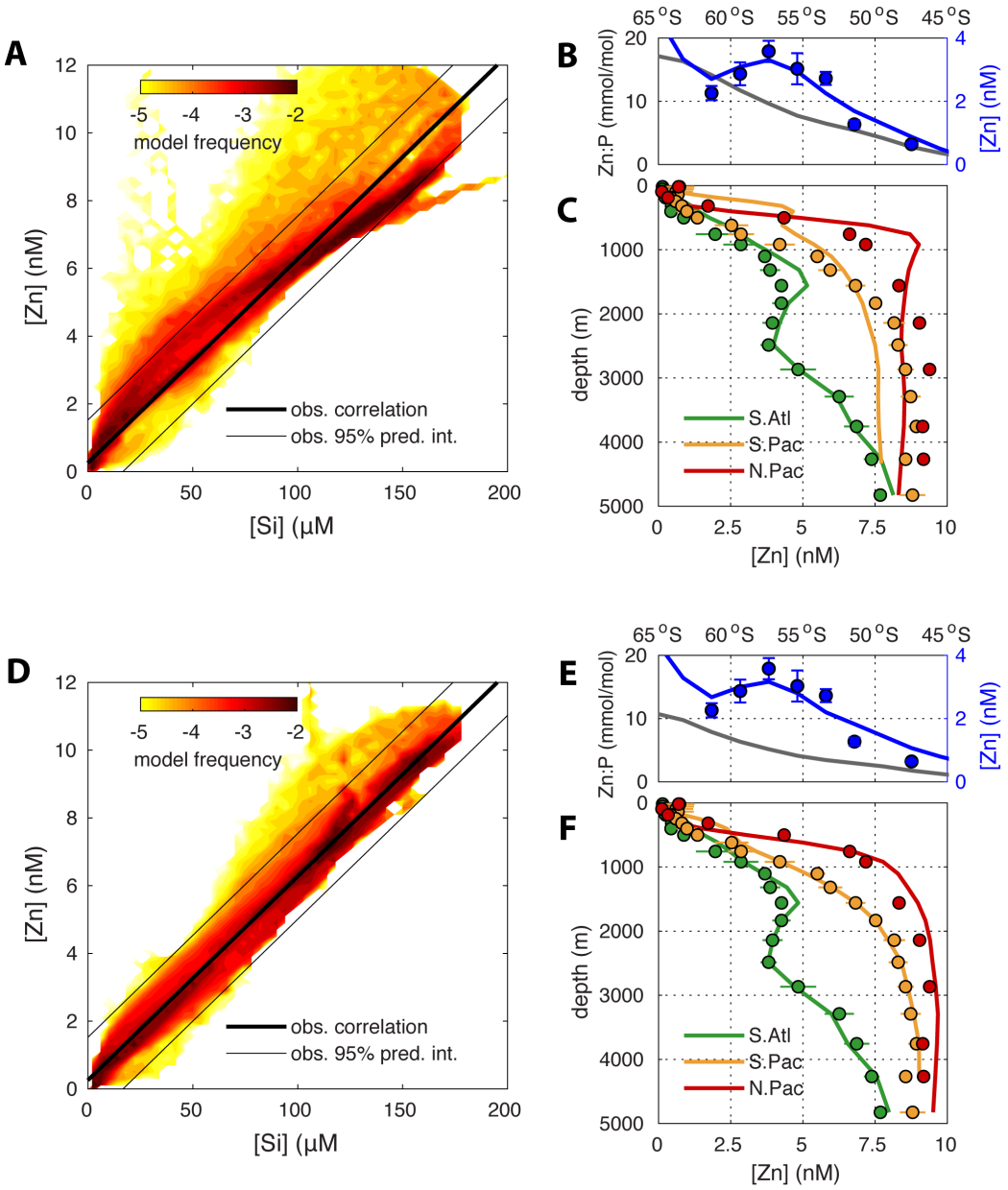

Figure 2. Mechanistic models of Zn cycling. (**A-C**) Model representing the Southern Ocean Zn-Si hypothesis, with optimized surface Zn uptake. (**D-F**) Model that resolves reversible scavenging of Zn onto sinking particles. Models are evaluated against the observed Zn vs. Si correlation (**A,D**), Southern Ocean surface distribution (**B,E**), and Atlantic and Pacific profiles (**C,F**). In **A** and **D**, the colormap shows the log fraction of the ocean volume with [Si] and [Zn] that fall within 1μM x 0.1nM bins. In B, C, E and F, dots are observed [Zn] ± 1.S.D. (*4, 9, 13, 31*) and lines are corresponding model results, averaged within small spatial regions (*15*).

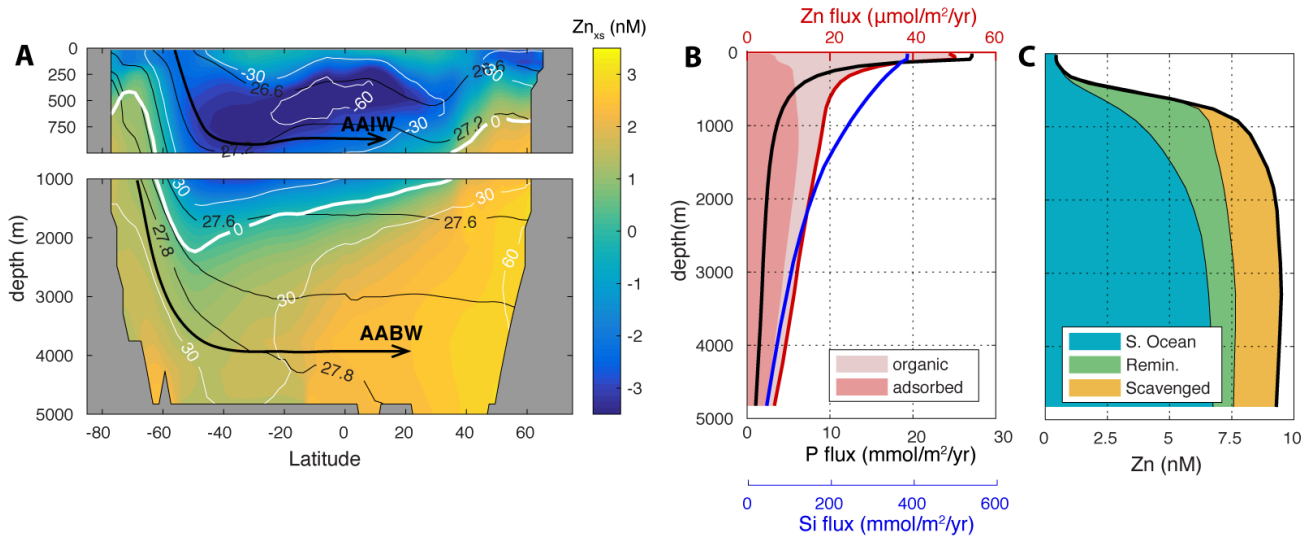

Figure 3. Holistic understanding of the model Zn cycle. A) The stoichiometric tracers Zn_{xs} (colormap) and Si_{xs} (white contours) measure the excess or deficit or Zn and Si relative to PO_4, and illustrate the relationship between the three nutrient cycles in our model. Both tracers show distinctive signatures circulated by AAIW and AABW from the Southern Ocean, and similar modifications along isoycnals outside of the Southern Ocean. **B**) Vertical flux profiles of P, Si and Zn. Organic Zn attenuates over depth like P, but adsorbed and organic components sum to a flux profile that is more similar to Si. **C**) Simulated North Pacific Zn (site analyzed in Fig. 1) is divided into a component circulated from the Southern Ocean, and components accumulated from remineralization and scavenging.

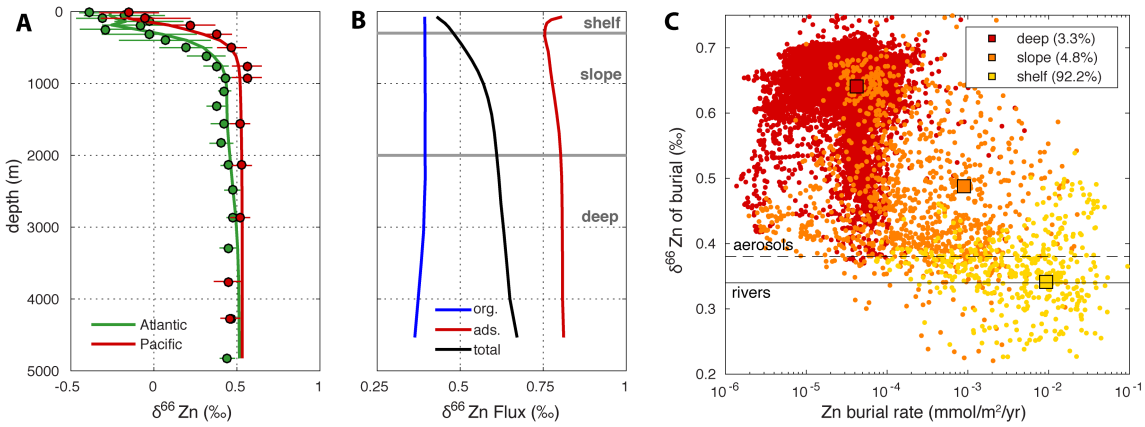

Figure 4. Zn isotope distribution and mass balance. A) Model fit to observed δ^{66}Zn profiles in the Atlantic and Pacific Oceans. **B**) Simulated isotopic composition of organic, adsorbed and total particulate fluxes. The decrease in δ^{66}Zn towards the surface in (**A**) results from the flux of heavy adsorbed Zn to the deep ocean. **C**) Relationship between Zn burial rate in sediments, computed offline from high-resolution topography and estimates of carbon burial (*15*), and δ^{66}Zn of the flux to seafloor. Square symbols integrate across shelf (0-200m), slope (200-2000m) and deep ocean (>2000m) regions. Most burial occurs in shallow shelf regions, where light organic Zn dominates the sinking flux (**B**), allowing the total δ^{66}Zn sink to match the source from aerosol and river inputs.

Supplementary Materials

Materials and Methods
Supporting Discussion
Figs S1 to S9
Tables S1 to S3

Supplementary Materials for

Biological uptake and reversible scavenging of zinc in the global ocean

Thomas Weber*, Seth John, Alessandro Tagliabue, Tim DeVries

correspondence to: t.weber@rochester.edu

This PDF file includes:

1. Materials and Methods

1.1 Circulation model

Our diagnostic (Section 1.2) and mechanistic (Section 1.3) models calculate tracer transport using most recent configuration of the observationally constrained Ocean Circulation Inverse Model (OCIM, (*32*)). This model simulates the three-dimensional general circulation at a horizontal resolution of 2°x2°, and on 24 depth levels with vertical resolution ranging from 30m in the surface to 500m in the deep ocean. Flow fields are optimized to fit a range of passive and transient tracers (temperature, salinity, ^{14}C, CFCs). Because this model reproduces the density structure and watermass ages of the ocean interior more accurately than dynamical models, it is ideal for distinguishing between the physical and biogeochemical controls on large-scale nutrient distributions ((*18*)). Annual-mean OCIM flow fields are stored as a matrix (**A**), allowing fast steady-state global simulations using the Transport Matrix Method (*33*).

1.2 Zn component analysis

To test whether the similar distribution of Zn and Si in Southern Ocean watermasses can explain their global covariation despite their contrasting remineralization behavior (*12*), we conducted a nutrient component analysis on observed profiles of Zn. Observed Zn (Zn_{obs}) at a given location in the ocean interior outside of the Southern Ocean, defined here as north of 40°S and deeper than 100m, can be defined as the sum of two components:

$$Zn_{obs} = Zn_{circ} + Zn_{accum} \quad (1)$$

Zn_{circ} represents the concentration of Zn that was passively circulated to the site from the surface or the Southern Ocean. It is therefore similar to the traditional definition of "preformed nutrient" (circulated from the surface), except it also accounts for the supply of Southern Ocean sourced nutrients at depth. We note that for subsurface Zn distributions, the supply from the Southern Ocean dwarfs the supply from the surface, so this component is described as "Southern Ocean sourced" in the main text. The second component, Zn_{accum}, represents the Zn that has accumulated in watermasses since they last past the boundaries at 100m and 40°S. Our goal is to isolate and quantify the two components.

Zn_{circ} is quantified by propagating observed "boundary" Zn concentrations (Zn_B) from the surface and the 40°S boundary into the ocean interior, without modification except by mixing. This is achieved by dividing the circulation matrix (**A**) into "boundary propagator" ($\mathbf{A_B}$) and "interior mixing" ($\mathbf{A_I}$) components (*33*), and solving the following continuity equation by matrix inversion for the steady state distribution of Zn_{circ}:

$$\frac{dZn_{circ}}{dt} = \mathbf{A_I} Zn_{circ} + \mathbf{A_B} Zn_B \quad (2)$$

Because the distribution of Zn is sparsely sampled, we mapped Zn_B statistically by applying the linear correlation between Zn and Si in the Southern Ocean (Fig. 1a) to the well-sampled distribution of Si (*34*). Zn_{accum} is then calculated as the difference between Zn_{obs} and Zn_{circ}.

Uncertainty in Zn_{accum} was quantified using a Monte Carlo method to repeat our calculation 10,000 times while propagating measurement uncertainty in Zn_{obs}, and uncertainty in Zn_{circ} that is introduced during the statistical mapping procedure. Each iteration randomly samples probability distributions for the slope and intercept of the Zn vs. Si correlation (Fig. 1a) and applies those parameters to map Zn_B and calculate Zn_{circ}. At the location of interest outside the Southern Ocean, a profile of Zn_{obs} is generated by randomly sampling a Gaussian distribution at each depth, defined by the reported mean and error of the observations. We present Zn_{circ} and Zn_{accum} profiles as the mean and standard deviation of the 10,000 individual iterations.

The "Southern Ocean hypothesis" states that Zn is globally coupled to Si by their similar distributions in AAIW and AABW formation regions, and otherwise Zn cycles identically to other soft-tissue nutrients like PO_4^{3-} (*12*). To test this, we repeated our analysis (Eqs 1-2) to isolate the components of PO_4^{3-} and Si that accumulated from organic matter decomposition (P_{accum}) and opal dissolution (Si_{accum}), to compare to Zn_{accum}. If the depth structure of Zn_{accum} is similar to P_{accum}, our analysis would support the Southern Ocean hypothesis. On the other hand, if it has a similar depth structure to Si_{accum}, our analysis would indicate that other mechanisms contribute to coupling Zn and Si in the global ocean. Because the global distributions of PO_4^{3-} and Si are well characterized compared to Zn, these analyses were only conducted once using World Ocean Atlas 2013 (WOA13) annual-mean distributions (*34*). Our analysis was applied at two locations in the Pacific Ocean:

(i) The "Sampling and Analysis of Fe" (SAFe) site in the North Pacific Ocean at 140°S, 35°N (Fig. 1b-d).
(ii) The Eastern Tropical South Pacific Ocean, between 85°W-105°W along ~13°S, sampled by GEOTRACES cruise GP16 (Fig. S1).

These locations were chosen because they are both largely ventilated from the Southern Ocean, and the transit timescale from the Southern Ocean to these sites is relatively long (*35*). This allows time for a strong Zn_{accum} signal to develop, with a clearly defined vertical structure that can be compared to P_{accum} and Si_{accum}. The Atlantic Ocean is rapidly ventilated by NADW from the north and Southern Ocean watermasses from the south, so develops a weaker Zn_{accum} signal without a clear vertical structure (indistinguishable from zero in most of the water column).

1.3 Mechanistic model of P, Si and Zn cycles

We coupled simple biogeochemical models of P, Si and Zn cycling to OCIM to test the mechanisms that control the global distribution of Zn.

P cycle: The oceanic P cycle is simulated following the OCMIP protocol (*36*). It resolves inorganic PO_4 and dissolved organic phosphorous (DOP), which are governed by the following continuity equations:

$$\frac{dPO_4}{dt} = \mathbf{A}PO_4 - J_{up}(PO_4) - \frac{\partial}{\partial z}F_{POP} + k_{DOP}DOP \quad (3)$$

$$\frac{dDOP}{dt} = \mathbf{A}DOP + \sigma J_{up}(PO_4) - k_{DOP}DOP \quad (4)$$

The first terms on the right hand side of Eqs 3 and 4 represent physical transport of PO_4^{3-} and DOP respectively (Section 1.1), while the remaining terms represent biogeochemical processes. $J_{up}(PO_4)$ is the net biological uptake of PO_4^{3-} by primary production in the euphotic zone, represented by restoring surface (top 75m, two model layers) concentrations towards their observed values. Fraction σ of the net uptake is routed towards DOP, which undergoes first-order decay at rate k_{DOP} back to PO_4^{3-}. Fraction (1-σ) of net PO_4^{3-} is routed to an implicit particulate organic phosphorous (POP) pool that remineralizes through the water column, represented by the vertical divergence (-$\partial/\partial z$) of the POP flux (F_{POP}). F_{POP} is assumed to attenuate over depth (z) following a power-law relationship with exponent b (*37*):

$$F_{POP}(z) = F_{POP}(z_{eu}).(z/z_{eu})^b \quad (5)$$

Here, $F_{POP}(z_{eu})$ is the export flux of POP at the base of the euphotic zone, i.e. the integral of $(1-\sigma)J_{up}(PO_4)$ over the top 75m. We do not resolve POP burial in sediments. Instead all POP reaching the seafloor remineralizes back into the bottom grid cell, representing a "closed system" with no sources and sinks of PO_4^{3-} to/from the ocean as whole.

The model defined by Eqs 3-5 can be solved directly for the steady state distributions of PO_4^{3-} and DOP using Newton's Method. Parameter values for k_{DOP} and σ were taken from previous studies (*38*), whereas the remineralization exponent b was optimized to minimize the volume-weighted RMSE between simulated PO_4^{3-} and the observed WOA13 annual-mean distribution (Table S1-S2, Fig. S2). The resulting model achieves R^2=0.95 compared to the global observations.

Si cycle: The oceanic Si cycle is simulated following previous studies (*11*), and is governed by the following continuity equation:

$$\frac{dSi}{dt} = \mathbf{A}Si - J_{up}(Si) - \frac{\partial}{\partial z}F_{bSi} \quad (6)$$

Net biological uptake, $J_{up}(Si)$, is simulated by restoring surface Si towards WOA13 observations, and transfers Si to an implicit biogenic opal (*bSi*) pool. Remineralization of *bSi* through the water column is represented as the vertical divergence of an exponential flux profile that attenuates over length scale H_{Si}:

$$F_{bSi}(z) = F_{bSi}e^{\frac{z-z_{eu}}{H_{Si}}} \quad (7)$$

Again, we assume a closed system and solve this model directly for the steady state distribution of Si using Newton's Method. The length scale H_{Si} was optimized to minimize the volume-weighted deviation from WOA13 (Table S1, Fig. S2), and the resulting model achieves R^2=0.97 compared to observations.

Zn cycle: Our model simulates the physical circulation, biological cycling, and chemical speciation/scavenging of Zn, and aims to determine the combination of these processes that is most consistent with observations. The continuity equation for total Zn (sum of all species) is:

$$\frac{dZn}{dt} = \mathbf{A}Zn - J_{up}(Zn) - \frac{\partial}{\partial z}F_{POZn} + J_{sc}(Zn) \quad (8)$$

Speciation of this total Zn tracer is resolved implicitly, by solving a reversible ligand binding reaction for the equilibrium partition between free *Zn'* and complexed *ZnL (16)*. This approach assumes that the binding reactions proceed faster than other processes, and is common practice in global models of trace metal cycling (*12, 39*). Two parameters must be specified to solve the system: The ligand concentration L, which we assume is

spatially uniform at 1nM (*16, 40*), and the conditional stability constant K_{cond}, which is treated as adjustable (see Section 1.4). The speciation model predicts that the majority of Zn is ligand-bound in the surface ocean, and unbound in the deeper ocean where concentrations greatly exceed the ligand concentration (Fig. S6).

We assume that biological Zn uptake, $J_{up}(Zn)$ in Eq. 8, is coupled stoichiometrically to $J_{up}(PO_4)$, because Zn and PO_4^{3-} both are assimilated into soft organic tissue. Based on observations from culture studies (*7*) we assume that phytoplankton can only access Zn^{2+}, which is linearly related to *Zn'* by $Zn^{2+}=Zn'/a_{Zn}$, and we use a "two-site model" to represent the Zn:P uptake ratio as a function of Zn^{2+} availability:

$$J_{up}(Zn) = \left(R_{Zn}\frac{Zn^{2+}}{Zn^{2+}+k_{Zn}} + c_{zn}Zn^{2+}\right)J_{up}(P) \quad (9)$$

Here, R_{Zn} is the maximum Zn:P ratio for the "saturating" portion of the two-site model and k_{Zn} determines the degree of "frugality" when *Zn'* is scarce, whereas c_{zn} is the slope of Zn:P vs. *Zn'* in the linear portion of the two-site model. All three are treated as free parameters, and optimized to best fit the global Zn distribution (Section 1.4-1.5).

After uptake, organic Zn is exported from the surface as particles. Due to the similar cellular distribution of Zn and P in organelles, particulate organic Zn is assumed to remineralize over depth exactly the same as POP, i.e. following the functional form in Eq. 5 and using the same flux attenuation exponent (*b*) from the optimized P cycle model.

In Eq. 8, $J_{sc}(Zn)$ represents the source or sink of Zn due to reversible scavenging onto organic particles. We use an implicit reversible scavenging model (*19*) to simulate the net effect of uncomplexed *Zn'* adsorbing onto particles, sinking of the adsorbed phase, and desorption back to the dissolved phase. The model assumes that a fast equilibrium is reached between adsorption and desorption, allowing the concentration of particle-adsorbed Zn (Zn_{ads}) to be solved based on the local particle abundance and a partition coefficient K_D:

$$Zn_{ads} = \frac{K_D POC}{K_D POC+1}Zn' \quad (10)$$

We assume that *Zn'* adsorbs only to organic particles (*9*), represented by the concentration of particulate organic carbon (*POC*), and not to mineral phases such as SiO_2, $CaCO_3$, MnO_2 and Fe_2O_3. *POC* is derived from the flux profile POP, an assumed particle sinking velocity w_{sink}, and Redfield stoichiometry:

$$POC = 106\frac{F_{POP}}{w_{sink}} \quad (11)$$

The source or sink of total Zn due to reversible scavenging is then given by the flux divergence of Zn_{ads}:

$$J_{sc}(Zn) = -\frac{\partial}{\partial z}(w_{sink}Zn_{ads}) \quad (12)$$

By combining equations 10-12 and noting that the fraction of Zn' in the adsorbed phase is always <<1, it can be seen that $J_{sc}(Zn)$ is not sensitive to the assumed sinking velocity of particles, as demonstrated by ref. (*41*). The sign of the reversible scavenging term is controlled by the local vertical gradient of *Zn'* and divergence of the particle flux profile. In the top 100-200m where Zn concentrations increase rapidly with depth, $J_{sc}(Zn)$ is usually a sink of Zn. In deeper waters, the attenuation of the particle flux results in a net Zn source from scavenging.

As with PO_4^{3-} and Si, we assume that all organic and adsorbed Zn reaching the seafloor is remineralized in the bottom grid cell, and do not resolve sources of Zn to the

ocean. Instead, we specify a fixed global-mean Zn concentration of 5.38nM, which we derived by applying the observed relationship with Si (Fig. 1a) to the WOA13 annual-mean Si distribution to constrain the oceanic Zn inventory.

1.4 Zn model configurations and optimization

We designed two configurations of our Zn model to test different mechanisms that are hypothesized to control the global Zn distribution. The first configuration (SOC) is designed to test the "Southern Ocean hypothesis" (*12*), which states that rapid Zn drawdown in the Southern Ocean results in a Si-like surface distribution in watermass formation regions that propagates into the ocean interior, but otherwise Zn cycles exactly like PO_4^{3-}. In the SOC configuration, the scavenging term $J_{sc}(Zn)$ in Eq. 8 is set to zero, resulting in a model with four free parameters: three controlling Zn:P uptake stoichiometry (R_{Zn}, k_{Zn}, c_{Zn}) and one controlling Zn speciation (K_{cond}). The second model configuration (SCAV) is designed to test the hypothesis that adsorption onto sinking particles enhances the Zn flux to the deep ocean relative to PO_4^{3-}, contributing to its Si-like deep concentration maximum. In the SCAV configuration, $J_{sc}(Zn)$ is represented by Eqs 10-12, which adds a single free parameter, K_D, to the model.

In both model configurations, the governing free parameters (4 in SOC, 5 in SCAV) were optimized within reasonable limits (Table S2) to minimize the discrepancy between the simulated and observed Zn distribution (Section 1.5). Remaining discrepancies are therefore indicative of structural deficiencies in the model (i.e. missing processes), rather than parameterization errors. If a model cannot reproduce the observations well even after parameter optimization, we assume the hypothesis it represents can be rejected.

1.5 Data constraints

We chose not to assess the model configurations based on a point-wise comparison to all available Zn data. Zn is still much more sparsely mapped than PO_4^{3-} and Si, and the Atlantic Ocean contributes the vast majority of the current data (*4*). A comparison that weights each data point equally might therefore select a parameter set that can match the Atlantic Zn distribution well, but fails in the Pacific. Instead we selected nine constraints for this comparison that capture the important large-scale features of the global Zn distribution. The locations of these profile constraints are shown in Fig. S3 and described briefly here:

1. **Southern Ocean surface:** Surface measurements (~5m) were taken from a transect between ~62°S and 48°S along the Greenwich Meridian (*13*), which reveals the Zn drawdown pattern in regions of AAIW formation.
2. **Antarctic Southern Ocean:** A profile was taken from 67°S on the Greenwich Meridian, in Antarctic Zone of the Southern Ocean (*13*).
3. **Subantarctic Southern Ocean:** A profile was taken from 52°S on the Greenwich Meridian, in the Subantarctic Zone of the Southern Ocean (*13*). Together, constraints 2 and 3 reveal the distribution of Zn over depth in the Southern Ocean.

4. **South Atlantic:** Profiles from the GEOTRACES GA02 and GA10 cruises were averaged at their intersection, between 25-48°W along 40°S. This composite profile reveals the distribution of Zn in AAIW and AABW watermasses as they leave the Southern Ocean.
5. **North Atlantic:** Profiles from the GEOTRACES GA02 and GA03 cruises were averaged at the intersection point of the two cruise tracks between 50-70°W and 27-37°N. This composite profile reveals the low [Zn] of North Atlantic Deep Water, and weak signature of AAIW reaching into the North Atlantic.
6. **Indian Ocean:** Profiles from the GEOTRACES GI04 cruise were averaged North of the Equator.
7. **Eastern Tropical South Pacific:** Profiles from the GEOTRACES GP16 cruise were averaged between 84°W-104°W along ~12°S (*31*).
8. **Northeast Pacific:** A profile was taken from the SAFe site (140°W, 35°N) at the boundary between Subarctic and Subtropical gyres in the North Pacific Ocean (*9*). Together, constraints 7 and 8 trace the development of a deep Zn concentration maximum along the path of AAIW in the Pacific Ocean.
9. **Subarctic North Pacific:** Four profiles were averaged along Line P in the Subarctic Northeast Pacific (*21*). In this region Zn concentrations are decoupled slightly from Si, counter to the global trend (Fig. S3), providing an important constraint on the differences between their elemental cycles.

For each of the nine constraints, we took the RMS error between observed and simulated [Zn] and divide by the mean observed Zn, yielding a non-dimensional measure of model-data mismatch for each constraint, which are then summed into an overall cost function. Our optimization procedure seeks the parameter set that minimizes this cost function.

1.6 Sensitivity tests

We considered alternative processes that might reconcile the SOC model with observations. In each case, we conducted a simple sensitivity test to examine their effect on the Zn distribution. Results of these tests are discussed in Section 2.2, and illustrated in Fig. S5.

Hydrothermal source: gradual accumulation of hydrothermal Zn along the conveyor belt circulation might account for the deep Zn maxima (relative to PO_4) in the Pacific Ocean, without needing to invoke the reversible scavenging mechanism. We tested this hypothesis by conducting a sensitivity simulation in which a hydrothermal Zn source is added to the SOC configuration of our model. The Zn input rate is proportional to the optimized hydrothermal ^{3}He source of ref. (*42*), with a Zn:^{3}He ratio of 3.2×10^6 (*17*). This results in a global hydrothermal Zn source of 1.93Gmol/yr that is similar to the global extrapolation of ref (*17*) (1.75±0.35Gmol/yr). In our sensitivity test, this source is balanced by "burying" a fraction of the particulate Zn that reaches seafloor sediments, and the fraction was tuned to maintain a global-mean [Zn] of 5.4μM. All other parameters were held at the optimized values from the previous version of the model.

Variable remineralization: Recent evidence suggests that the remineralization length scale of particulate organic matter varies spatially in the ocean (*18, 43*). Given that Zn export has a different spatial pattern to P export, it is possible that remineralization alone could decouple the two cycles and potentially result in deeper Zn accumulation. We conducted a sensitivity test in which a spatially varying pattern of the remineralization exponent (*b*) was specified based on the particle transfer efficiency results of ref. (*18*) and other parameters were held at the previous optimized values.

O_2-dependent scavenging: Sulfide precipitation in low oxygen microenvironments has been invoked as a mechanism by which particles transfer trace metals to in hypoxic regions of the water column (*20*). To test whether this mechanism is a viable alternative scavenging mechanism – as opposed to adsorption and desorption to/from particle surfaces – we conducted simulations in which scavenging was confined to hypoxic waters. This was achieved by smoothly reducing K_D to zero where O_2 exceeds 50μM, which has the net effect of transferring Zn to particles when $[O_2]$<50μM, and releasing the scavenged Zn deeper in the watercolumn when $[O_2]$> 50μM. K_D and all other parameters were then re-optimized to best match our observational constraints. We conducted further experiments in which the $[O_2]$ threshold was raised to 100μM, 150μM and 200μM, to determine how widespread scavenging must be reproduce the observed Zn distribution.

1.7 Elimination experiments

Having arrived at an optimum model that best explains the global Zn observations, we attempted to quantify the contributions of reversible scavenging and elevated biological uptake in the Southern Ocean to the global Zn distribution. Each process was removed from the model (or "switched off") in turn, and its importance quantified by the degradation of the model of the performance (in terms of R^2). Starting with the optimized SCAV model configuration, we first switched off scavenging by setting K_d to 0 without altering other parameters. This prevents vertical redistribution of Zn from intermediate to deep waters, and degrades the model fit to global observations from R^2=0.93 (optimum model) to 0.81. Elevated Southern Ocean uptake was switched off by capping the Zn:P uptake ratio at 5mmol/mol – the highest ratio observed outside of the Southern Ocean. This allows leakage of Zn from the Antarctic Zone of the Southern Ocean and into AAIW, degrading the model fit to observations to R^2=0.83. The similar degradation of model performance suggests that the two processes make approximately equal contributions to the global Zn distribution.

1.8 Isotope modeling

We followed the methods outlined in ref (*9*) to simulate the distribution of δ^{66}Zn, defined as:

$$\delta^{66}Zn = \left({}^{66}Zn/{}^{64}Zn \Big/ R_{std} - 1 \right) . 1000 \qquad (13)$$

where R_{std} is the $^{66}Zn/^{64}Zn$ ratio in an accepted standard. Briefly, the distribution of the dominant isotope ^{64}Zn is assumed to be the same as the total Zn tracer, then Eq. 8 is used to independently simulate a tracer representing ^{66}Zn. The total oceanic ^{66}Zn inventory is set assuming a global-mean $\delta^{66}Zn$ of 0.5‰ (*23*), and the isotopes are fractionated during biogeochemical processes. Kinetic fractionation during biological uptake is represented by defining:

$$J_{up}(^{66}Zn) = \alpha_{prod} \frac{^{66}Zn'}{^{64}Zn'} J_{up}(Zn) \quad (14)$$

where α_{prod} is the uptake fractionation factor. Equilibrium fractionation during complexation and reversible scavenging are represented by assuming a constant $\delta^{66}Zn$ offset (ε) between the chemical species involved in each process:

$$\varepsilon_{lig} = \delta^{66}ZnL - \delta^{66}Zn' \quad (15)$$

$$\varepsilon_{scav} = \delta^{66}Zn_{ads} - \delta^{66}Zn' \quad (16)$$

Given the simulated distribution of ^{64}Zn and values of ε_{lig} and ε_{scav}, Eqs. 15-16 can be solved to determine the fraction of ^{66}Zn in each gridcell that is in the $^{66}Zn'$, ^{66}ZnL and $^{66}Zn_{ads}$ phases. Biological uptake (Eq. 14) and scavenging (Eq. 12) rates can be cast in terms of total ^{66}Zn, allowing the equivalent equation to Eq. 8 to be solved directly for the steady state distribution of ^{66}Zn using Newton's method, and $\delta^{66}Zn$ to be computed using Eq. 13. We note that from a modeling perspective the value of R_{std} is arbitrary, as long as the same value is used consistently, as discussed by ref. (*44*) from the perspective of nitrogen cycle modeling. Following that convention, we select R_{std}=1.

After importing optimized parameters and rates from the total Zn model, only three free parameters remain in the ^{66}Zn model: α_{prod}, ε_{lig}, and ε_{scav}. These parameters were optimized within reasonable ranges (Table S2) to best match four observed profiles of $\delta^{66}Zn$ from the North Atlantic, South Pacific, North Pacific and Southern Oceans (Locations 2,5,7 and 8 in Section 1.5). Again, a non-dimensional cost is calculated for each constraint, and the optimization procedure seeks the parameter set that minimizes the sum of the individual costs.

We note that preferential complexation of ^{64}Zn (negative ε_{lig}) and preferential scavenging of heavy ^{66}Zn (positive ε_{scav}) produce similar overall effects in the model. Both result in the transfer of heavy Zn into the adsorbed phase and its removal from the upper ocean, resulting in an increase in $\delta^{66}Zn$ over depth. The optimization procedure selects for a stronger fractionation during complexation than adsorption, which allows the model to better match the shape of observed $\delta^{66}Zn$ profiles and is consistent with new measurements from the Subtropical Pacific Ocean (Section 1.10). However, the same qualitative trend can be reproduced with fractionation during scavenging only, and our inferences about the global isotope budget remain unchanged regardless of which process is responsible for isotope fractionation.

1.9 Benthic Zn burial

Our Zn cycle model assumes a closed system, so does not explicitly simulate sources and sinks of Zn to and from the ocean. However, our results can be used to draw inferences about the global isotopic Zn budge. Our goal is to determine whether the isotopic signature of Zn burial in seafloor sediments (the dominant sink) matches the relatively

well-constrained $\delta^{66}Zn$ of fluvial, atmospheric, and hydrothermal inputs (*23*).To achieve this, rates and isotope ratios of Zn burial were estimated "offline" by combining our optimized model results with independent estimates of particulate carbon burial.

Carbon burial was estimated following the method of (*24*), first mapping carbon deposition onto seafloor sediments at high resolution by combining satellite estimates of particulate organic carbon (POC) export, an assumed vertical flux profile, and the ETOPO2 global bathymetry map. This is preferable to computing the seafloor POC flux in our coarse resolution biogeochemical model, which lacks the resolution to capture continental margin bathymetry and coastal phytoplankton blooms, so would dramatically underestimate POC deposition on shelf sediments. The high-resolution deposition map was then combined with an empirical relationship for burial efficiency (*24*) to estimate carbon burial rates, and interpolated to our model grid. Finally, carbon burial rates were converted to Zn burial based on the simulated Zn:POC flux ratio at the seafloor, combining both particulate organic and adsorbed Zn components.

The procedure was repeated for both Zn isotopes, to calculate the isotopic signature of burial in each grid cell, revealing a striking negative correlation between the $\delta^{66}Zn$ of particulate Zn reaching the seafloor and its burial rate (Fig. 4c). That is, while the burial flux is heavier than mean ocean dissolved $\delta^{66}Zn$ over most of the areal extent of the seafloor, burial $\delta^{66}Zn$ was isotopically lighter in a restricted regions with high organic burial flux. Burial rates of each isotope were integrated to compute the flux-weighted regional and global mean $\delta^{66}Zn$ of buried Zn (Fig. S9). Uncertainty in the spatial pattern of particulate organic carbon export was propagated into the calculation by repeating our calculation using the nine satellite export estimates assembled by ref. (*18*), which combine three estimates of NPP and three algorithms for the particle export ratio.

The isotope effect of biological Zn uptake (α_{prod}) is relatively unconstrained – it has only been measured for a few cultured phytoplankton species, and likely varies as a function of external conditions including Zn and Fe concentrations (*45, 46*). We therefore tested whether our isotope budget results are sensitive to the value of this parameter, by repeating the full burial calculation with α_{prod} set to 1 (no fractionation) and to 0.992 (0.8‰ fractionation, the upper limit in ref. (*45*)) rather than the optimized value in Table S2. These experiments yielded global $\delta^{66}Zn$ sinks of 0.33‰±0.05‰ and 0.38‰±0.04‰ respectively, which are indistinguishable from the original value of 0.36‰±0.04‰. Our results are therefore not sensitive to the exact degree of isotope fractionation during biological uptake. This is due to the near-complete consumption of Zn in most of the regions where burial rates are high, meaning that the $\delta^{66}Zn$ of the organic flux is determined by the isotopic composition of upwelling dissolved Zn, rather than by α_{prod}.

1.10 Measurements of isotope fractionation during ligand-binding

The equilibrium isotope effect between ligand-bound Zn and free Zn was determined by analyzing ligand-bound Zn collected from 500 m and 850 m in the North Pacific Ocean at Station ALOHA (22.75 N, 158 W) in July 2015. Organic ligands were extracted from 20L seawater samples onto 1 g Bond-Elut-ENV solid phase extraction (SPE) column according to the methods outlined in ref (*47*). Samples were eluted with methanol and evaporated, then analyzed for $\delta^{66}Zn$ according to the anion exchange purification and

isotope analysis methods of ref (*48*). To calculate the equilibrium isotope effect, we assumed that $\delta^{66}Zn$ captured on the SPE reflects the entire ligand pool, even though recoveries were only a small portion the total, and that ligand-bound Zn accounted was 1 nM of the total Zn pool (*40*). Total dissolved [Zn] and $\delta^{66}Zn$ at the sample depths were interpolated from measurements at the North Pacific SAFe site (*49*). Predicted isotope effects (ε_{lig}) were -1.42 ‰ and -0.90 ‰ for samples at 500 m and 800 m, respectively.

2. Supporting Discussion

2.1 Comparison to previous results and model limitations

The results of our SOC model are somewhat inconsistent with a previous study using a similar model configuration (*12*), which did not report a systematic bias towards high Zn in intermediate waters and low Zn in deep waters. This discrepancy likely stems from two important differences between the studies.

First, we have used an optimization method to constrain the most realistic values for PO_4 and Si remineralization parameters (Section 1.3, Table S1), within the context of our circulation model, whereas ref (*12*) uses previous literature values. Compared to our optimized values, their selections (b=0.85, H_{Si}=1000m) result in deeper PO_4 (and therefore Zn) remineralization and shallower Si remineralization, making their remineralization depths more similar.

Second, we employ the observationally-constrained OCIM circulation model (Section 1.1), which assimilates circulation tracers to improve the representation of watermass distributions and ventilation timescales, relative to traditional dynamical models. The model used in ref (*12*) suffers a number of biases in watermass structure, including production of bottom water at ~50°S in the Southern Ocean rather than near the Antarctic coastline, and over-production of North Pacific Intermediate Water (*50, 51*). Combined with potential remineralization biases, this might lead to unrealistically strong coupling of Zn and Si cycles.

Despite its realistic watermass distributions and ventilation rates, the OCIM model suffers its own limitations. First, it is an annual-mean model that lacks a seasonal cycle of circulation and biological nutrient uptake. This may introduce biases because in the real ocean, nutrient concentrations subducted into the ocean interior in wintertime at mid/high latitudes are likely higher than summertime concentrations we use as constraints. Our model may therefore carry too little Zn in intermediate waters, causing us to under-estimate the degree of scavenging required to match the observed distribution. Second, the coarse resolution of OCIM (2°x2° horizontal, 24 vertical layers) means it cannot resolve continental shelf regions where much of the Zn burial occurs. For this reason we have used previous interpolated high-resolution estimates of organic matter burial in those regions when estimating the isotope ratio of Zn burial.

2.2 Sensitivity test results

Results of sensitivity simulations (Section 1.6) are compared to observations in Fig. S5.

Hydrothermal source: In our model, hydrothermal Zn inputs produce local-scale enrichments near ocean ridges, but do not produce the global-scale redistribution of Zn from intermediate to deep waters needed to match observations. We note that our circulation model does not always correctly capture the transport trajectory of hydrothermal plume, due to poorly resolved deep zonal currents. This is particularly apparent in the South Pacific, where the model predicts a hydrothermal Zn peak at ~2500m to the East of the East Pacific Rise (Fig. S5, panel 7), whereas observations

indicate transport of hydrothermal Zn to the West only (*17*). Nevertheless, it is clear that accumulation of hydrothermal Zn along the Meridional Overturning Circulation conveyor, which well represented in our circulation model (*32*) cannot account for the deep accumulation of Zn in the North Pacific. We also note that in order to balance the hydrothermal Zn source, our model requires that almost 100% of particulate Zn reaching the seafloor must be buried. Such efficient burial of organic matter is not supported by observations, suggesting that the hydrothermal source is too large and the Zn:^{3}He ratio derived from the East Pacific Rise (*17*) may not be globally applicable. Upcoming observations targeting hydrothermal systems, combined with further model development may be able to place better constraints on this Zn source in the future.

Variable remineralization: Accounting for spatial variations in organic matter remineralization depth is able to somewhat improve the model's performance in the North Pacific, where slightly more Zn accumulates in deep waters compared to the original SOC configuration. However, this comes at the expense of weaker performance in the Southern Ocean, where Zn too concentrated. These effects likely result from deep remineralization in the Southern Ocean (*18*) where the majority of Zn export occurs. This traps Zn within the deep Southern Ocean, and concentrates it in AABW that flows northwards into the Pacific. Therefore, even though slower surface Zn uptake may restore the correct Southern Ocean distribution, this would re-weaken the model performance in the North Pacific, as AABW would contain less Zn. Given that the original SOC configuration already matches Southern Ocean [Zn] very well, and our component analysis suggests that deep Zn accumulation occurs outside the Southern Ocean (Fig. 1), it is unlikely that variable remineralization depth can simultaneously improve model performance in all regions.

O_2-dependent scavenging: When scavenging is confined to waters with [O_2] lower than 50μM, an unrealistically sharp Zn maximum forms in the lower oxycline of North Pacific Ocean (1000-2000m), and deep ocean concentrations are under predicted throughout the Indian and Pacific basins as a whole. Similar, but less extreme, biases are found when the O_2 threshold is raised to 100μM and 150μM. Only when $[O_2]_{crit}$ reaches 200μM can the model approach the same good fit to data that is achieved in the SCAV configuration, with [O_2]-independent scavenging. These results demonstrate that Zn scavenging is ubiquitous through the ocean and not confined to low oxygen waters, suggesting that sulfide precipitation is not a viable scavenging mechanism.

3. Supplementary Figures

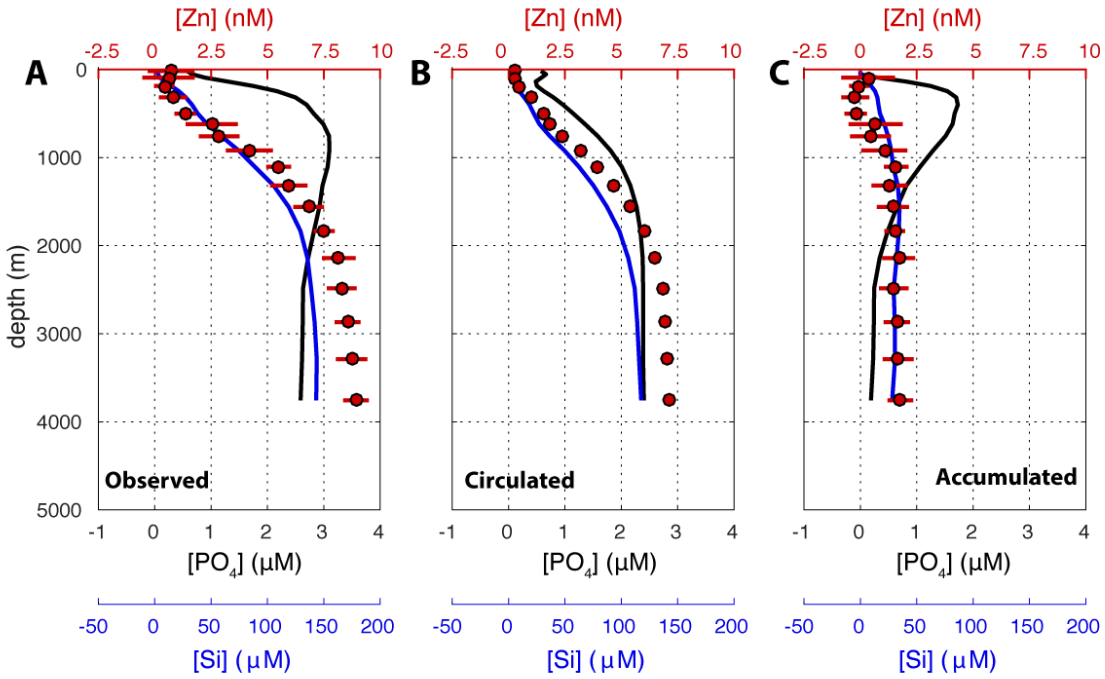

Figure S1. Nutrient component analysis repeated for the Eastern Tropical South Pacific Ocean. As in Fig. 1, observed profiles of Zn, PO_4^{3-} and Si (**A**) are divided into a "circulated" component (**B**) that was transported from the Southern Ocean or surface ocean, and an "accumulated" component (**C**) that has built up since leaving those regions.

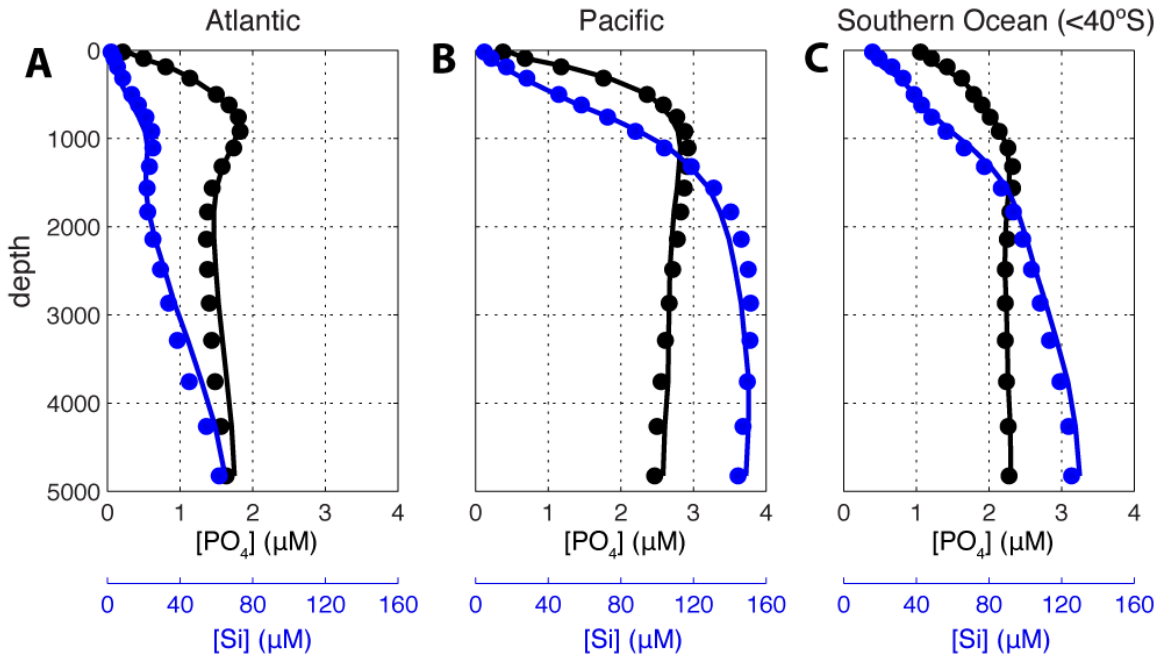

Figure S2. Validation of PO_4 and Si models. Basin-mean profiles of PO_4 and Si for the (**A**) Atlantic, (**B**) Pacific and (**C**) Southern Oceans, compared between our optimized model (lines) and World Ocean Atlas 2013 annual-mean observations (dots). The close match between model and observations (R^2=0.95 for PO_4, 0.97 for Si) reflects both the realistic circulation of the OCIM model, and the optimized remineralization parameters.

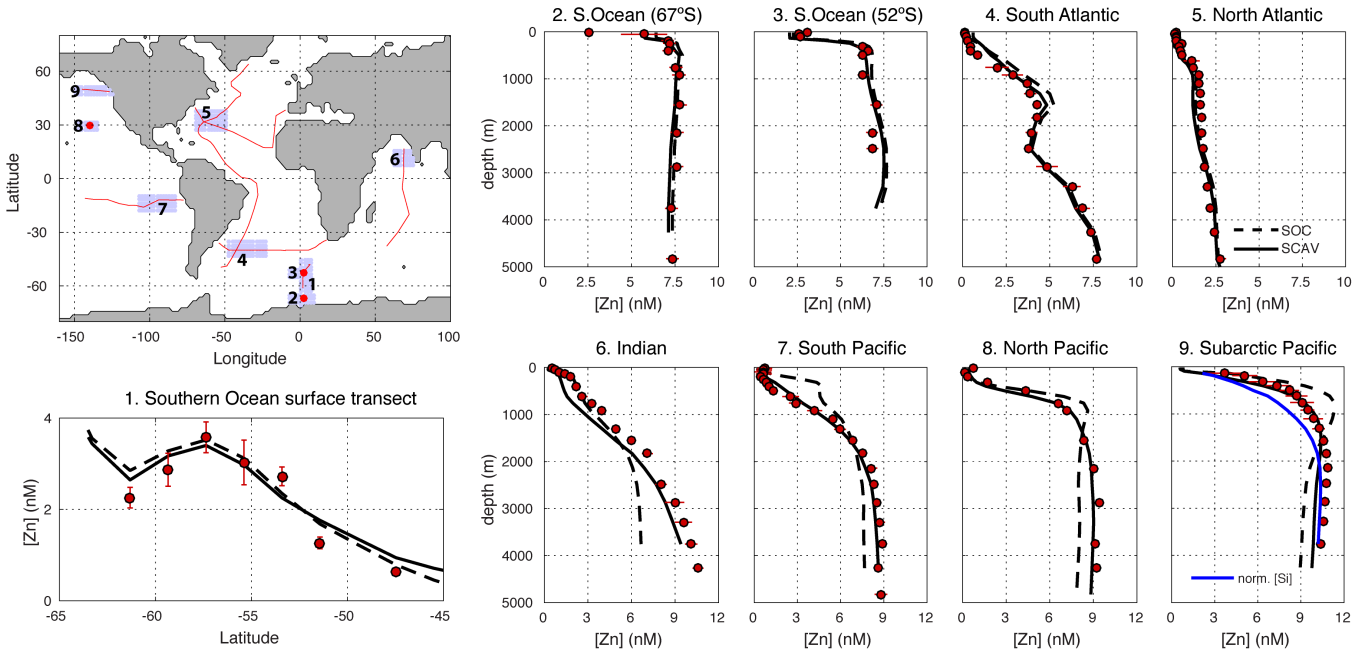

Figure S3. Data constraints used in Zn model optimization. Top left: map of constraint locations, showing cruise tracks for transect data (red lines) and location of individual profile data (red dots). Numbered blue boxes represent the regions within which observations and model output were averaged for comparison, and are defined in Section 1.5. Numbered panels show the comparison between observations and the two model configurations (SOC and SCAV, Section 1.4) in each region. In most regions, Zn is observed to have a very similar depth structure to Si. In the Subarctic North Pacific (bottom right panel), observed Si is shown in blue (normalized by the deep-ocean Zn:Si ratio) to demonstrate the slight decoupling of Zn from Si observed in this region, which is again captured realistically by the SCAV model.

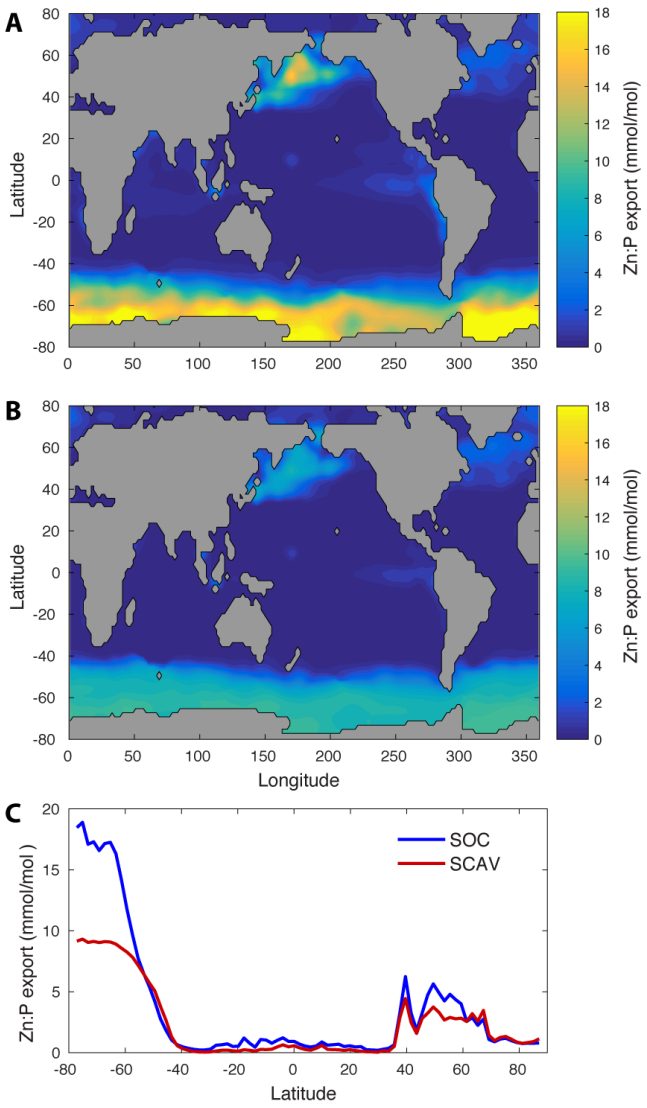

Figure S4. Biological Zn:P uptake. Depth-integrated ratio of biological Zn:P export from the surface ocean (0-75m), predicted in the (**A**) SOC and (**B**) SCAV model configurations. (**C**) Zonal-mean export ratio is compared between the two models.

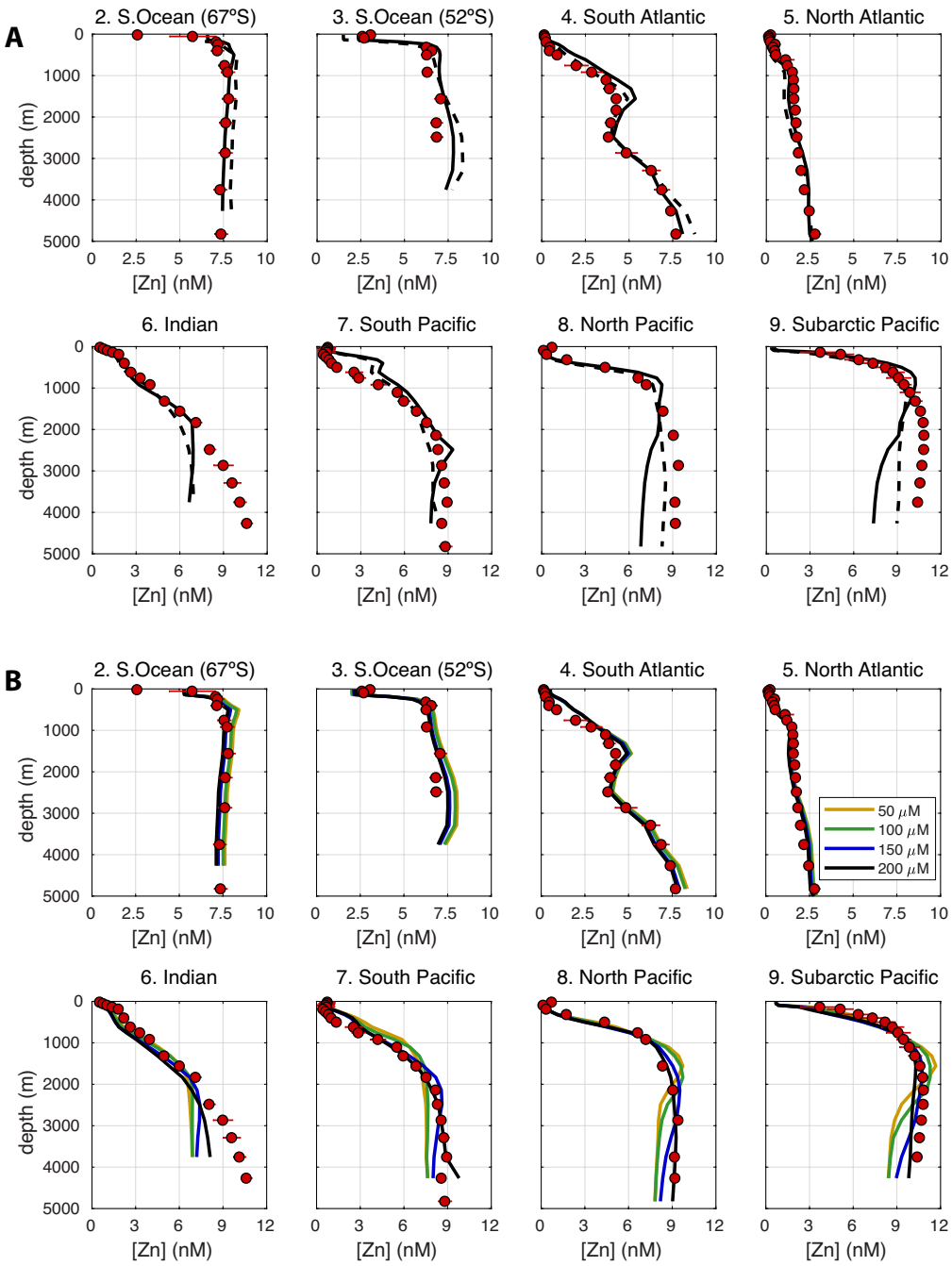

Figure S5. Sensitivity test results. A. Results of two sensitivity simulations in which additional processes are added to the SOC model configuration: hydrothermal Zn inputs (solid black line) and variable remineralization length scale of organic matter (dashed black line). **B.** Results of sensitivity tests using the SCAV configuration, in which scavenging was confined to waters with [O_2] below four different threshold values. Observed concentrations are shown as red dots in all panels. See Fig. S3 for numbered model-data comparison locations, and Section 2.2 for discussion of results.

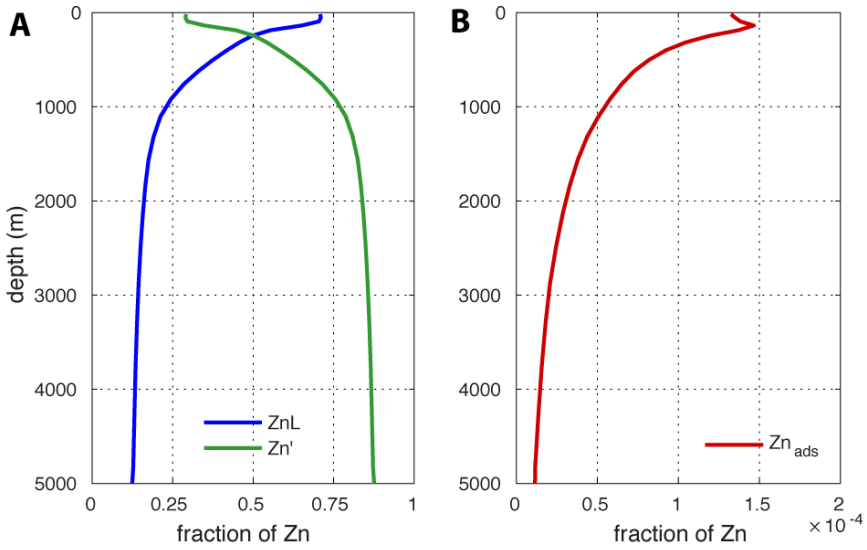

Figure S6. Speciation of Zn in the SCAV model configuration. Global-mean profiles show fraction of total Zn in the ligand-bound and free phases (**A**), and in the adsorbed phase (**B**). Note different x-axis scales between **A** and **B**, because adsorbed Zn compromises a very small fraction of total exchangeable Zn.

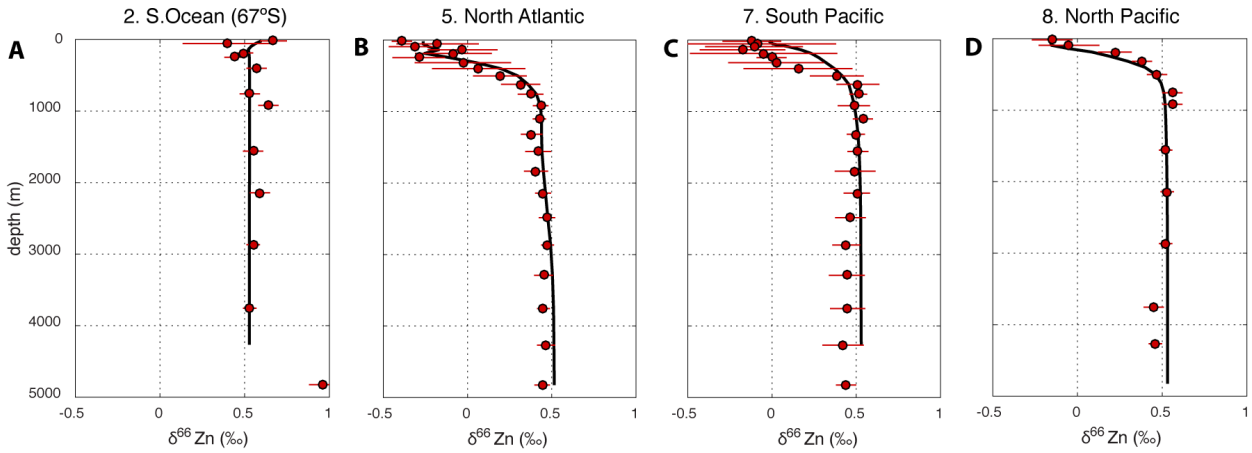

Figure S7. δ^{66}Zn constraints used in isotope model optimization. Fractionation effects for biological uptake, ligand-binding, and adsorption were optimized to minimize the misfit between simulated and observed δ^{66}Zn profiles in the (**A**) Southern, (**B**) Atlantic, (**C**+**D**) Pacific Oceans. For data locations (numbered) see Fig. S3.

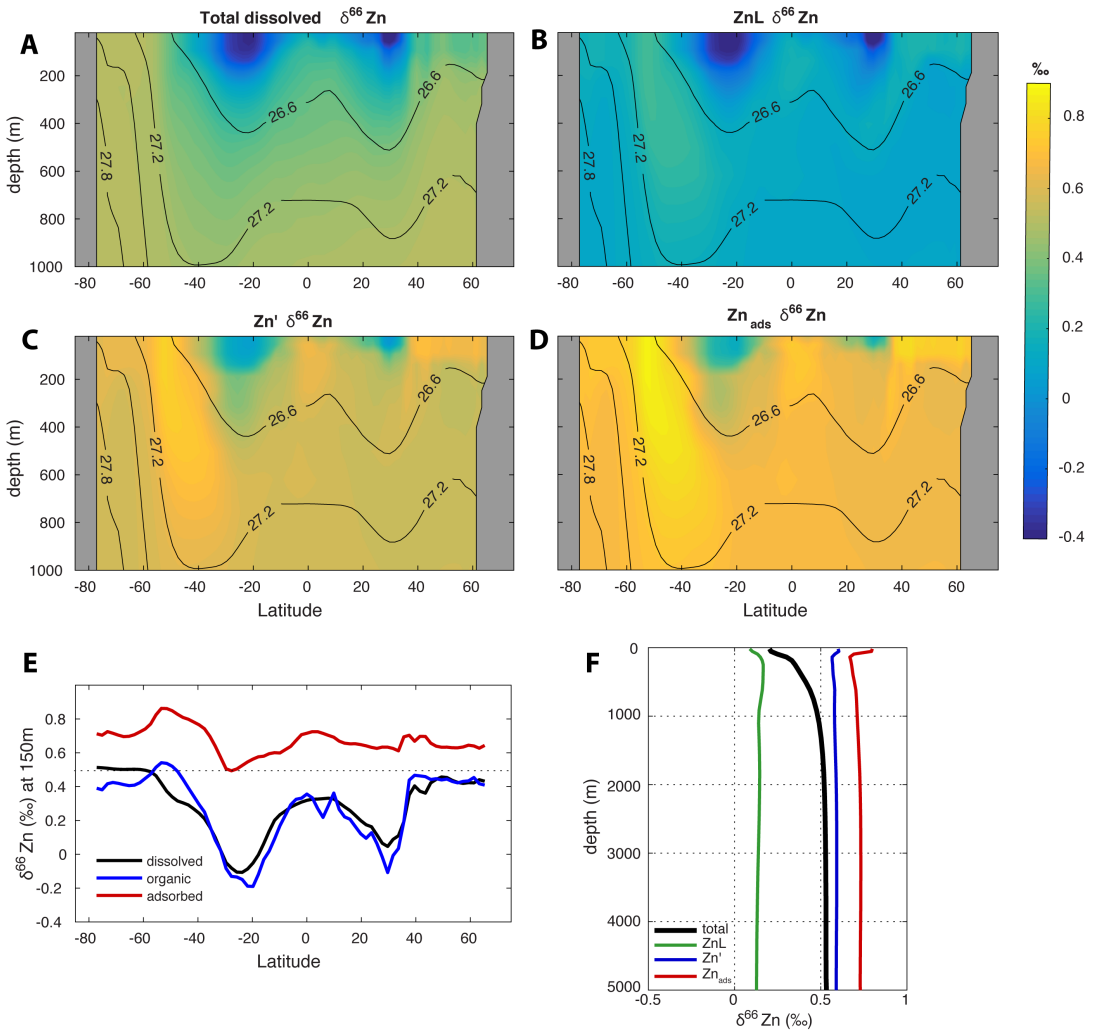

Figure S8. Isotopic composition of Zn species. A-D Zonal mean cross sections of δ^{66}Zn in the Pacific upper ocean (0-1000m) for (**A**) total, (**B**) ligand-bound, (**C**) free, and (**D**) adsorbed Zn. Preferential binding of the lighter isotope results in consistently lower δ^{66}Zn of ligand-bound ZnL (**B**), and higher δ^{66}Zn of unbound Zn' (**C**), relative to total dissolved Zn (**A**). Preferential scavenging of the heavy isotope further enriches δ^{66}Zn of particle-adsorbed Zn_{ads} (**D**). Sinking of adsorbed Zn therefore strips the upper ocean of heavy isotopes, resulting in low δ^{66}Zn through the low latitude thermocline. (**E**) Zonal mean δ^{66}Zn at 150m of dissolved (ZnL+Zn'), organic and adsorbed Zn. Quantitative consumption of Zn in the low latitude surface transfers the light signature to organic matter, demonstrated by the isotopic similarity of upwelling dissolved Zn (black line) and sinking organic Zn (blue line) at 150m. The distinct isotopic signatures of organic and adsorbed (red line) fluxes allows preferential removal of heavy isotopes from the upper ocean (by adsorbed Zn), while light isotopes are preferentially removed from the ocean as a whole (by burial of organic Zn). (**F**) Global-mean profiles of δ^{66}Zn. In the deep ocean, [Zn] greatly exceeds the ligand concentration, so unbound Zn' and adsorbed Zn_{ads} become isotopically more similar to total dissolved Zn over depth. The preferential

downwards flux of heavy isotopes is therefore curtailed in the deep ocean, which results in the relatively homogeneous profiles of $\delta^{66}Zn$ below ~1000m (Fig. 4a, S7).

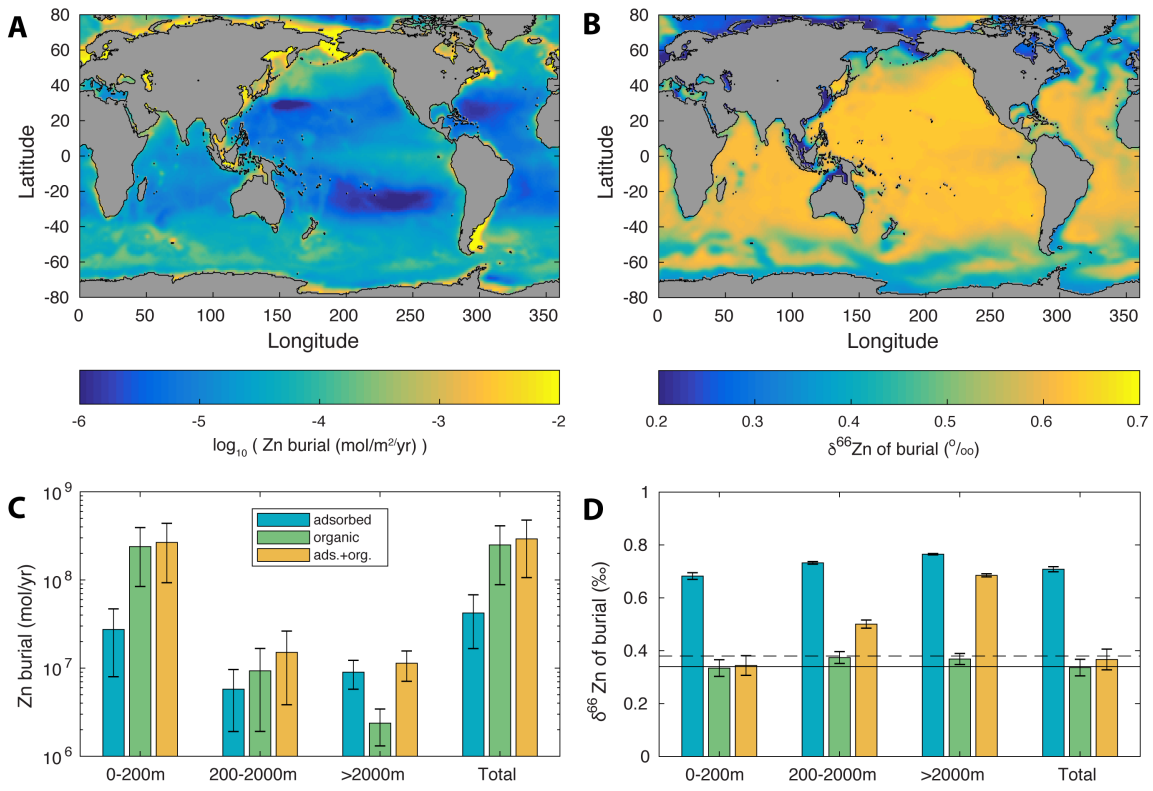

Figure S9. Calculation of δ^{66}Zn burial in seafloor sediments (background information for Fig. 4c). (**A**) Zn burial rates are mapped at high resolution by combining previous high resolution estimates of carbon burial with the Zn:C ratio of the simulated particle flux at the seafloor. (**B**) Simulated δ^{66}Zn of total particulate Zn (organic and adsorbed) at the seafloor, interpolated to the high resolution bathymetry. (**C**) Burial rates integrated across shelf (0-200m), slope (200-2000m) and deep ocean (>2000m) bathymetric regimes, and divided between adsorbed and organic components. (**D**) Integrated δ^{66}Zn of organic, adsorbed and total Zn burial in each bathymetric regime. Burial occurs disproportionately on shelves, where the light organic flux dominates (**C**), resulting in light δ^{66}Zn burial when integrated globally (**D**).

4. Supplementary Tables

Table S1. Parameters for mechanistic model of PO_4^{3-}, Si and Zn cycling. For free parameters of the Zn model, ranges represent the limits allowed during the optimization procedure. These are defined by expanding the ranges observed in the literature cited. The model must therefore select values that are of similar magnitude to observed values, but can explore parameter spaces slightly outside the observed range.

Symbol	Description	Value or allowed range	Reference or constraint
z_{eu}	Euphotic zone depth (biological uptake is only allowed above this depth)	75m	Ref. (*38*)
σ	Fraction of PO_4^{3-} uptake routed to DOP	0.5	Ref. (*38*)
k_{DOP}	Decomposition rate of DOP	0.5 $year^{-1}$	Ref. (*38*)
b	Flux attenuation exponent for particulate P and Zn	0.92	Optimized to fit WOA13 PO_4^{3-} climatology
H_{Si}	Flux attenuation length scale for biogenic silicate	1640m	Optimized to fit WOA13 Si climatology
L	Zn binding ligand concentration	1nM	Ref. (*40*)
K_{cond}	Conditional stability for Zn binding	10^9-10^{11} M^{-1}	Ref. (*16*)
a_{Zn}	Ratio of Zn' to Zn^{2+}	2.1	Ref. (*52*)
R_{Zn}	Maximum Zn:P for saturating portion of two-site model	10^{-3}-$5x10^{-2}$ mol:mol	Refs. (*7, 12*)
k_{Zn}	Half saturation constant for saturating portion of two-site model	$5x10^{-6}$-$5x10^{-4}$ μM	Refs. (*7, 12*)
c_{Zn}	Slope of Zn:P vs. Zn^{2+} for linear portion of two-site model	0.1-10 μM^{-1}	Refs. (*7, 12*)
K_D	Partition coefficient for Zn scavenging onto POC	Unbounded, but evaluated based on fraction of Zn in adsorbed phase (see text)	-
w_{sink}	Sinking speed of particles, applied to adsorbed Zn	50mday^{-1} (results insensitive to value)	Ref. (*41*)
α_{prod}	Kinetic fractionation factor for biological uptake of ^{66}Zn relative to ^{64}Zn	0.9992-1	Ref. (*45*)
ε_{lig}	Equilibrium isotope effect for ligand binding (Eq. 15)	-1.5 to 0‰	Section 1.8
ε_{scav}	Equilibrium isotope effect for adsroption (Eq. 16)	0-0.6‰	(*9*)

Table S2. Optimized values for free model parameters for the SOC and SCAV model configurations (Section 1.4).

Parameter	SOC configuration	SCAV configuration
$\log_{10}(K_{cond})$	10.42	10.47
R_{Zn}	18.2×10^{-3} mol:mol	9.1×10^{-3} mol:mol
k_{Zm}	2×10^{-4} µM	3×10^{-5} µM
c_{Zn}	0.8 μM^{-1}	0.7 μM^{-1}
K_D	-	7.07×10^{-4} $(\mu gC)^{-1}$
α_{prod}	-	0.9998
ε_{lig}	-	-0.42‰
ε_{scav}	-	0.19‰

Table S3. Root mean square error for the SOC and SCAV model configurations following optimization, for each regional constraint (Fig. S3).

Region (Fig. S3)	RMSE (µM)	
	SOC configuration	SCAV configuration
1. Southern Ocean transect	0.43	0.44
2. Southern Ocean 67ºS	0.62	0.51
3. Southern Ocean 52ºS	0.97	0.89
4. North Atlantic	0.49	0.44
5. South Atlantic	0.44	0.24
6. Tropical Indian Ocean	1.45	0.85
7. Tropical South Pacific	1.68	0.59
8. North Pacific	1.28	0.51
9. Subarctic North Pacific	1.61	0.80
TOTAL	1.03	0.59

References and Notes

1. B. S. Twining, S. B. Baines, The trace metal composition of marine phytoplankton. *Annual review of marine science* **5**, 191-215 (2013).
2. F. M. M. Morel *et al.*, Zinc and Carbon Co-Limitation of Marine-Phytoplankton. *Nature* **369**, 740-742 (1994).
3. K. W. Bruland, G. A. Knauer, J. H. Martin, Zinc in Northeast Pacific Water. *Nature* **271**, 741-743 (1978).
4. E. Mawji *et al.*, The GEOTRACES Intermediate Data Product 2014. *Marine Chemistry* **177**, 1-8 (2015).
5. C. Mahaffey, S. Reynolds, C. E. Davis, M. C. Lohan, Alkaline phosphatase activity in the subtropical ocean: insights from nutrient, dust and trace metal addition experiments. *Frontiers in Marine Science* **1**, (2014).
6. Y. Shaked, Y. Xu, K. Leblanc, F. M. M. Morel, Zinc availability and alkaline phosphatase activity in Emiliania huxleyi: Implications for Zn-P co-limitation in the ocean. *Limnology and Oceanography* **51**, 299-309 (2006).
7. W. G. Sunda, S. A. Huntsman, Feedback Interactions between Zinc and Phytoplankton in Seawater. *Limnology and Oceanography* **37**, 25-40 (1992).
8. M. J. Ellwood, K. a. Hunter, The incorporation of zinc and iron into the frustule of the marine diatom Thalassiosira pseudonana. *Limnology and Oceanography* **45**, 1517-1524 (2000).
9. S. G. John, T. M. Conway, A role for scavenging in the marine biogeochemical cycling of zinc and zinc isotopes. *Earth and Planetary Science Letters* **394**, 159-167 (2014).
10. B. Twining, S. Nodder, A. King, Differential remineralization of major and trace elements in sinking diatoms. *Limnol. Oceanogr* **59**, 689-704 (2014).
11. M. Holzer, F. W. Primeau, T. DeVries, R. Matear, The Southern Ocean silicon trap: Data-constrained estimates of regenerated silicic acid, trapping efficiencies, and global transport paths. *Journal of Geophysical Research: Oceans* **119**, 313-331 (2014).
12. D. Vance *et al.*, Silicon and zinc biogeochemical cycles coupled through the Southern Ocean. 1-6 (2017).
13. Y. Zhao, D. Vance, W. Abouchami, H. J. W. de Baar, Biogeochemical cycling of zinc and its isotopes in the Southern Ocean. *Geochimica et Cosmochimica Acta* **125**, 653-672 (2014).
14. J. L. Sarmiento, N. Gruber, M. a. Brzezinski, J. P. Dunne, High-latitude controls of thermocline nutrients and low latitude biological productivity. *Nature* **427**, 56-60 (2004).
15. Materials and methods are available as supplementary materials at the Science website
16. T. Kim, H. Obata, Y. Kondo, H. Ogawa, T. Gamo, Distribution and speciation of dissolved zinc in the western North Pacific and its adjacent seas. *Marine Chemistry* **173**, 330-341 (2015).
17. S. Roshan, J. Wu, W. Jenkins, *Long-range transport of hydrothermal dissolved Zn in the tropical South Pacific*. (2016), vol. 183.

18. T. Weber, J. A. Cram, S. W. Leung, T. DeVries, C. Deutsch, Deep ocean nutrients imply large latitudinal variation in particle transfer efficiency. *Proceedings of the National Academy of Sciences*, 201604414 (2016).
19. M. P. Bacon, R. F. Anderson, Distribution of Thorium Isotopes Between Particulate Forms in The Deep Sea. *Journal of Geophysical Research* **87**, 2045-2056 (1982).
20. D. J. Janssen *et al.*, Undocumented water column sink for cadmium in open ocean oxygen-deficient zones. *Proceedings of the National Academy of Sciences* **111**, 6888-6893 (2014).
21. D. J. Janssen, J. T. Cullen, Decoupling of zinc and silicic acid in the subarctic northeast Pacific interior. *Marine Chemistry* **177**, 124-133 (2015).
22. T. M. Conway, S. G. John, The biogeochemical cycling of zinc and zinc isotopes in the North Atlantic Ocean. *Global Biogeochemical Cycles* **28**, 1111-1128 (2014).
23. S. H. Little, D. Vance, C. Walker-Brown, W. M. Landing, The oceanic mass balance of copper and zinc isotopes, investigated by analysis of their inputs, and outputs to ferromanganese oxide sediments. *Geochimica Et Cosmochimica Acta* **125**, 673-693 (2014).
24. J. P. Dunne, J. L. Sarmiento, A. Gnanadesikan, A synthesis of global particle export from the surface ocean and cycling through the ocean interior and on the seafloor. **21**, 1-16 (2007).
25. S. H. Little, D. Vance, J. McManus, S. Severmann, Key role of continental margin sediments in the oceanic mass balance of Zn and Zn isotopes. *Geology* **44**, 207-210 (2016).
26. S. Pichat, C. Douchet, F. Albarede, Zinc isotope variations in deep-sea carbonates from the eastern equatorial Pacific over the last 175 ka. *Earth and Planetary Science Letters* **210**, 167-178 (2003).
27. M. Kunzmann *et al.*, Zn isotope evidence for immediate resumption of primary productivity after snowball Earth. *Geology* **41**, 27-30 (2013).
28. M. L. Pons *et al.*, A Zn isotope perspective on the rise of continents. *Geobiology* **11**, 201-214 (2013).
29. M. A. Brzezinski, D. M. Nelson, The Annual Silica Cycle in the Sargasso Sea near Bermuda. *Deep-Sea Res Pt I* **42**, 1215-1237 (1995).
30. L. Bopp *et al.*, Multiple stressors of ocean ecosystems in the 21st century: projections with CMIP5 models. (2013).
31. S. G. John, J. Helgoe, E. Townsend, Biogeochemical cycling of Zn and Cd and their stable isotopes in the Eastern Tropical South Pacific. *Marine Chemistry*, (2017).
32. T. DeVries, The oceanic anthropogenic CO2 sink: Storage, air‐sea fluxes, and transports over the industrial era. *Global Biogeochemical Cycles* **28**, 631-647 (2014).
33. S. Khatiwala, A computational framework for simulation of biogeochemical tracers in the ocean. *Global Biogeochemical Cycles* **21**, (2007).
34. H. E. Garcia *et al.*, *World Ocean Atlas 2013, Volume 4 : Dissolved Inorganic Nutrients (phosphate, nitrate, silicate)*. (2013), vol. 4, pp. 27 pp-27 pp.

35. T. DeVries, F. Primeau, Dynamically and Observationally Constrained Estimates of Water-Mass Distributions and Ages in the Global Ocean. *Journal of Physical Oceanography* **41**, 2381-2401 (2011).
36. R. G. Najjar *et al.*, Impact of circulation on export production, dissolved organic matter, and dissolved oxygen in the ocean: Results from Phase II of the Ocean Carbon-cycle Model Intercomparison Project (OCMIP-2). *Global Biogeochemical Cycles* **21**, (2007).
37. J. H. Martin, G. A. Knauer, D. M. Karl, W. W. Broenkow, VERTEX: carbon cycling in the northeast Pacific. *Deep Sea Research Part A, Oceanographic Research Papers* **34**, 267-285 (1987).
38. T. DeVries, J.-H. Liang, C. Deutsch, A mechanistic particle flux model applied to the oceanic phosphorus cycle. *Biogeosciences* **11**, 5381-5398 (2014).
39. P. Parekh, Modeling the global ocean iron cycle. *Global Biogeochemical Cycles* **18**, 1-16 (2004).
40. K. W. Bruland, Complexation of zinc by natural organic ligands in the central North Pacific. *Limnology and Oceanography* **34**, 269-285 (1989).
41. M. Siddall *et al.*, Towards explaining the Nd paradox using reversible scavenging in an ocean general circulation model. *Earth and Planetary Science Letters* **274**, 448-461 (2008).
42. M. Holzer *et al.*, Objective estimates of mantle 3He in the ocean and implications for constraining the deep ocean circulation. *Earth and Planetary Science Letters* **458**, 305 - 314 (2017).
43. C. M. Marsay, R. J. Sanders, S. a. Henson, K. Pabortsava, E. P. Achterberg, Attenuation of sinking particulate organic carbon flux through the mesopelagic ocean. (2014).
44. C. J. Somes *et al.*, Simulating the global distribution of nitrogen isotopes in the ocean. *Global Biogeochemical Cycles* **24**, 1-16 (2010).
45. S. G. John, R. W. Geis, M. a. Saito, E. a. Boyle, Zinc isotope fractionation during high-affinity and low-affinity zinc transport by the marine diatom Thalassiosira oceanica. *Limnology and Oceanography* **52**, 2710-2714 (2007).
46. M. Kobberich, D. Vance, Kinetic control on Zn isotope signatures recorded in marine diatoms. *Geochimica Et Cosmochimica Acta* **210**, 97-113 (2017).
47. R. M. Boiteau, J. N. Fitzsimmons, D. J. Repeta, E. A. Boyle, Detection of Iron Ligands in Seawater and Marine Cyanobacteria Cultures by High-Performance Liquid Chromatography-Inductively Coupled Plasma-Mass Spectrometry. *Analytical Chemistry* **85**, 4357-4362 (2013).
48. T. M. Conway, A. D. Rosenberg, J. F. Adkins, S. G. John, A new method for precise determination of iron, zinc and cadmium stable isotope ratios in seawater by double-spike mass spectrometry (vol 793, pg 44, 2013). *Anal Chim Acta* **801**, 97-97 (2013).
49. T. M. Conway, S. G. John, The cycling of iron, zinc and cadmium in the North East Pacific Ocean - Insights from stable isotopes. *Geochimica Et Cosmochimica Acta* **164**, 262-283 (2015).
50. J. C. Dutay *et al.*, Evaluation of ocean model ventilation with CFC-11: comparison of 13 global ocean models. *Ocean Model* **4**, 89-120 (2002).

51. S. C. Doney *et al.*, Evaluating global ocean carbon models: The importance of realistic physics. *Global Biogeochemical Cycles* **18**, (2004).
52. M. J. Ellwood, C. M. G. Van den Berg, Zinc speciation in the Northeast Atlantic Ocean. *Marine Chemistry* **68**, 295-306 (2000).